

Failure Prediction of Open-pit Mine Landslide Containing Complex Geological Structure using Inverse Velocity Method: A Case Study in West Open-Pit mine, Pingzhuang, China

Han Du

Tsinghua University

Danqing Song (✉ songdq2019@mail.tsinghua.edu.cn)

Tsinghua University

Research Article

Keywords: Failure time of landslide, Open-pit coal mine, Inverse velocity, Early warning, Field monitoring

Posted Date: June 24th, 2021

DOI: <https://doi.org/10.21203/rs.3.rs-573230/v1>

License: © ⓘ This work is licensed under a Creative Commons Attribution 4.0 International License.

[Read Full License](#)

1 Failure prediction of open-pit mine landslide containing complex geological structure
2 using inverse velocity method: A case study in West Open-Pit mine, Pingzhuang,
3 China

4 Han Du, Danqing Song*

5 Department of Hydraulic Engineering, State Key Laboratory of Hydrosience and Engineering,
6 Tsinghua University, Beijing, 100084, China

7 *Corresponding author at: Department of Hydraulic Engineering, State Key Laboratory of
8 Hydrosience and Engineering, Tsinghua University, Beijing 100084, China. Tel./Fax. +86-10-
9 62794910. E-mail address: danqingsonglzu@163.com (DQ. Song).

10 **Abstract**

11 In the field of open-pit geological risk management, landslide failure time prediction is one of the
12 important topics. Based on the analysis of displacement monitoring data, the inverse velocity method
13 (IVM) has become an effective method to solve this issue. In order to improve the reliability of landslide
14 prediction, four filters were used to test the velocity time series, and the effect of landslide failure time
15 prediction was compared and analyzed. The IVM is used to predict the failure time of open-pit coal mine
16 landslide. The results show that the sliding process of landslide can be divided into three stages based on
17 the IVM: the initial attenuation stage (regressive stage), the second attenuation stage (progressive stage),
18 the linear reduction stage (autoregressive stage). The accuracy of the IVM is closely related to the
19 measured noise of the monitoring equipment and the natural noise of the environment, which will affect
20 the identification of different deformation stages. Compared with the raw data and the exponential
21 smoothing filter (ESF) models, the fitting effect of short-term smoothing filter (SSF) and long-term
22 smoothing filter (LSF) in the linear autoregressive stage is better. A slope displacement pixel difference

23 method based on fitting accuracy and field monitoring signals is proposed to determine the point onset-
24 of-acceleration (OOA) that is very important role for landslide prediction. A stratified prediction method
25 combining SSF and LSF is proposed. The prediction method is divided into two levels, and the
26 application of this method is given.

27 **Keywords:** Failure time of landslide; Open-pit coal mine; Inverse velocity; Early warning; Field
28 monitoring

29

30 **1. Introduction**

31 Landslides are one of the most common natural disasters and have a significant impact on people's
32 activities (Wu et al., 2018; Haque, 2019). Landslide stability is affected by many factors, such as rainfall
33 (Gao et al. 2017; Chen et al. 2020), earthquake (Fan et al. 2016; Song et al. 2020a,b), geological structure,
34 such as folds, discontinuities and faults (Kim et al. 2015); blasting (Liu et al. 2020), physical and
35 chemical weathering (Admassu et al. 2012; Chen and Song 2021), and excavation (Song et al. 2020a,b).
36 Rock mass movement and surface deformation are related phenomena caused by surface subsidence or
37 landslide in open-pit mines (Tarolli and Sofia 2016; López-Vinielles et al., 2020) (as shown in Fig1).
38 With the development of large-scale deep pit open-pit mining engineering activities, mine landslide
39 disasters continue to occur all over the world, posing a serious threat to open-pit mining and human social
40 safety (Ma et al. 2018; Liu et al., 2020). Under the condition that the production speed is fast and the
41 safety of workers and equipments must be guaranteed at the same time, the correct and reasonable
42 prediction of open-pit mine landslide can not only provide guidance for slope design and construction,
43 but also reduce the social and economic harm caused by engineering accidents. Landslide failure has
44 always been one of the most common geological disasters in open-pit mines, and landslide prediction

45 has always been an important topic in the field of geotechnical engineering (Zare Naghadehi et al. 2013;
46 Ma et al., 2018; Song et al., 2020c,d).

47 In recent years, many scholars have carried out a series of studies on the prediction time of landslide
48 failure (Fukuzono 1985; Voight 1989; Ventura et al., 2009). In the laboratory geomechanical model tests
49 and field tests, some methods can be used to predict the failure time of landslides (Bozzano et al. 2014;
50 Chen and Jiang 2020). Although the prediction methods for the general rule of failure mechanism and
51 time of all types of landslides do not yet exist, many achievements have been made in the previous
52 research work, and a large number of empirical derivation methods and related equations have been
53 obtained (Rose and Hungr 2007; Carlà et al. 2017). However, most analysis methods are regression
54 analysis based on displacement or strain time series before landslide failure, and finally obtain the
55 relationship related to some inherent properties of rock mass (Ventura et al., 2009). At present, the IVM
56 based on creep theory is one of the most widely used methods in the prediction of landslide failure time
57 (Dick et al. 2015). Fukuzono (1985) proposed the reverse velocity method, which provides a useful tool
58 for interpreting monitoring data and can better predict the final slope failure time. Rose and Hungr (2007)
59 used the IVM to predict the potential failure of rock slope in open-pit mines. Mufundirwa et al. (2010)
60 adopted IVM (IVM) to predict the failure time of rock mass and landslide. Based on this, SLO method
61 were proposed to predict the failure time of rock mass in Asamushi and Vaiont landslides. Osasan and
62 Stacey (2014) investigated the failure of mine slope and establish a landslide warning model by using
63 IVM. Carlà et al. (2017) predicted the time of different types of landslides using IVM, compared and
64 analyzed the applicability of the four IVM models, and deduced the general criteria for convenient data
65 smoothing processing. Zhou et al. (2020) introduced a controllable variable and proposed an improved
66 IVM, which can reduce the prediction error caused by the decrease of acceleration before failure.

67 Previous studies have shown that linear fitting of displacement time series by IVM is a simple and
68 effective tool for predicting landslide failure time. However, the process of inferring appropriate linear
69 trend lines and reliable fault predictions from inverse velocity diagrams is adversely affected by the noise
70 in the measurement. In addition, due to the complex geological structure of open-pit landslides, IVM has
71 certain limitations. For example, local slope movement, measurement error, human activities, rainfall etc
72 will have an impact on the displacement rate, which will seriously affect the reliability and accuracy of
73 the prediction results. Therefore, the application of IVM in time prediction of open-pit mines landslides
74 needs to be further discussed, and some analysis strategies and applicability in INM need to be studied.

75 In the field of landslide research, in-situ monitoring is a very important work to study the instability
76 characteristics and failure mechanism of landslide (Liu et al. 2020; Du et al. 2020). Interpretation of
77 monitoring data is one of the key points in predicting the timing of geomechanical failure or in assessing
78 the probability of imminent collapse of a rock slope (He et al. 2018). The instruments available for slope
79 monitoring in open-pit mines include precise measuring stations and prisms, inclinometers, global
80 positioning system (GPS) equipment and seismometers (Dick et al., 2015; Ma et al. 2018; Liu et al.
81 2020;). The methods of surface and subsurface monitoring, data collection and evaluation are
82 comprehensively described. A common method of interpreting the monitoring data is to convert the
83 measured values into rates (velocities), in general, slope failure is preceded by increased rates of
84 displacement, strain or microseismic activity, where displacement rates (velocities) are generally
85 considered to be the best indicator of the failure process (Severin et al. 2014). In recent years, many
86 efficient monitoring techniques have emerged. Ground-based radar is one of the most effective and
87 powerful monitoring technologies, which is very suitable for landslide monitoring requirements (Luzi,
88 2010; Mazzanti, 2011). Radar slope monitoring is widely used worldwide, such as slope stabilization

89 radar (SSR) and moving and surveying radar (MSR), which are currently used in many mines around the
90 world. In recent years, ground-based radar has been widely used in landslide monitoring, and ground-
91 based radar has made some achievements in landslide prediction (Bozzano et al., 2010; Dick et al., 2015;
92 Tommaso et al., 2017). However, in order to fully realize the effectiveness of radar in the prediction of
93 landslide failure in open-pit mines, it is necessary to establish a method that can efficiently predict the
94 slope failure time by combining radar displacement monitoring.

95 In this work, taking an open-pit mine coal landslide as an example, the Ground-based Synthetic Aperture
96 Radar monitoring system is used to monitor the displacement of the landslide, and the relevant
97 displacement data before and during the landslide are obtained. The inverse velocity method is used to
98 predict the sliding time of the landslide, which verifies the effectiveness of IVM in the prediction of the
99 landslide time of the open pit mine, and provides an important basis for the prevention and control of the
100 landslide and the mining of the open pit mine. The interference effects of engineering noise on IVM
101 landslide time prediction, including strong noise and weak noise, were discussed in detailed. Four kinds
102 of filters (Raw data, SSF, LSF, and ESF) are used to test the velocity time series, and the effect of
103 landslide failure time prediction is compared and analyzed. A slope shift pixel difference method based
104 on fitting accuracy and field monitoring signals is proposed to determine point OOA. A stratified
105 prediction method combining SSF and LSF is proposed, and its applicability is analyzed.

106

107 **2. Study area**

108 The topographic of Pingzhuang Town is subordinated to intramontane basin, which is located on the
109 north-eastward subhill ramp of Haer-nao Mountain. The perimeter of Pingzhuang Town contains the
110 largest lignite reserves in Eastern of Inner Mongolia Autonomous Region with an apparent reserve of

111 around 200 billion tonnes. With the increasing scale of open-pit mining, under the influence of a series
112 of factors such as open pit, underground joint excavation, fault and weak layer, the landslide disaster is
113 particularly prominent, which seriously threatens the safety production of open pit mine. There were
114 more than 40 landslides of different sizes at the top of the mining area, with a total volume of 4 million
115 cubic meters, which caused a series of safety production and geological environment problems in the
116 open-pit mine.

117 A massive landslide occurred on the afternoon of 17 April 2013 in West Pit, an open-cast coal mine
118 located approximately 6.73 km southwestern fringe of Yuanbao town, southeastern Inner Mongolia,
119 China (Fig. 2). Satellite remote sensing image of Pingzhuang West Open-pit Mine were shown in Fig. 3.
120 The front view and planar map of the landslide are shown in Fig. 4. Fig. 4 shows that after the occurrence
121 of the landslide, the sliding body accumulates in the upper part of the coal seam, resulting in coal pressing
122 phenomenon, which results in the failure of local coal seam mining. The landslide affected northern top
123 slope of the open pit, resulting in the suspend production. Pingzhuang coalfield is situated composite
124 zone between the Yinshan Mountains - Tianshan Mountains latitudinal structural belt and the
125 northeastern neocathaysian system of second subsidence belt, the northern foothill of the Yanshan
126 mountains of China. The region comprises a 405 m extra-thick siliciclastic sequence consists of quartz
127 arenite and shale, which makes up the JIUFOTANG Fm Group of Jurassic system. The transition to the
128 mantling volcanic sedimentation, which symbolizes the predominant lithosphere of YUANBAO SHAN
129 FUXIN Group, was determined by several distinct and extremely fluctuating categories of alteration of
130 underneath sandstone layers, central carboniferous, and overlying sandy-stone interval.

131

132 **3. Methodology**

133 3.1 Mathematical model of VMI landslide time prediction

134 The feedback dynamic result of the characteristic signal of an event in the past period is used to predict
135 the characteristic information of the event in the future period of time, and the method with predictive
136 ability input indexed by time is abstracted, which can be understood as a time series model. Saito
137 proposed an improved method for landslide time prediction based on the traditional creep theory, by
138 which the creep process was divided into three stages: average deformation, constant deformation and
139 accelerated deformation (Fig. 5). To make the displacement time series data more stable, Fukuzono (1985)
140 made improvement on this basis, and obtained that the logarithm of velocity and the logarithm of
141 acceleration were proportional. Under the constant loading condition of the slope, the time under the
142 corresponding time stamp of the landslide displacement can be expressed as follows:

143
$$\frac{d^2x}{dt^2} = a\left(\frac{dx}{dt}\right)^\alpha \quad (1)$$

144 where, the x is the displacement time series, (unit: m/s); T is the monitoring time (unit: s); a and α are
145 dimensionless constant parameters.

146 By comparing and analyzing the experimental results, Fukuzono (1985) determined that the value range
147 of the dimensionless parameter was between 1.5 and 2.2. The correlation between displacement rate and
148 landslide time can be expressed as follows:

149
$$\frac{1}{v} = [a \cdot (\alpha - 1)]^{\frac{1}{\alpha-1}} (t_f - t)^{\frac{1}{\alpha-1}} \quad (2)$$

150 where, v is the displacement change rate sequence, m/s; t_f is the predicted landslide time; t is the time
151 course of landslide evolution.

152 In addition, some scholars pointed out that both α and A can change with the change of time stamping,
153 and the different values range of α is directly related to the morphological change of the curve (as shown

154 in Fig. 6). When $\alpha > 2$, the curve shows a protruding shape. When $\alpha \in (1, 2)$, the curve is concave; When
 155 $\alpha = 2$, the curve is linear. When $\alpha = 2$, the landslide time can be calculated by the following formula:

$$156 \quad t_f = [t_2 \cdot \left(\frac{1}{v}\right)_1 - t_1 \left(\frac{1}{v}\right)_2] / \left[\left(\frac{1}{v}\right)_1 - \left(\frac{1}{v}\right)_2\right] \quad (3)$$

157 The above relation is expressed as a more universal relation that can better describe the failure rate of the
 158 slope, as follows:

$$159 \quad \frac{d^2x}{dt^2} = A \frac{dx}{dt}^\alpha \quad (4)$$

160 Where, $\frac{d^2x}{dt^2}$ and $\frac{dx}{dt}$ are displacement acceleration and acceleration respectively.

161 By substituting Equation (2) and (3) into Equation 4, we can get:

$$162 \quad t_f - t = \left[\frac{\frac{dx}{dt}^{(1-\alpha)} - \frac{dx_f}{dt}^{(1-\alpha)}}{A(\alpha - 1)} \right] \quad (5)$$

163 If the prediction of landslide time is taken into account, the expression mode of inverse multiplication
 164 element of velocity data at slope sliding is regarded as infinite in Eq. (5), and the linear model can be
 165 used as a reference for landslide time prediction when the intercept of X-axis is infinitely close.

166 The above time series prediction time model of landslide is obtained under ideal conditions, but in fact
 167 the model is limited by the interference caused by measurement error and equipment noise. In particular,
 168 the open-pit mine slope is usually affected by cyclical factors such as rainfall, groundwater, freeze-thaw
 169 of snow and ice, and artificial mining, etc. In this work, a mathematical model is built to eliminate
 170 engineering noise interference for landslide prediction, and noise is divided into the following two
 171 categories: (a) Instrumental noise (IN) of the measuring equipment, caused by the accuracy of the data
 172 collected by the equipment. (b) Environmental noise (EN) caused by environmental factors.

173 To avoid the dependence of single-point monitoring time series data and extract the periodicity of time
 174 as the feature, three smoothing filter algorithms are proposed to denoise the original velocity data. The

175 three models are as follows. Short-period easy shifting filter (SSF): the speed is expressed as following

176 Eq (6):

$$177 \quad \bar{v}_t = \frac{v_t + v_{t-1} + \mathbf{L} v_{t-(n-1)}}{n} \quad \mathbf{n=3} \quad (6)$$

178 LSF model: the velocity is expressed as following Eq (6):

$$179 \quad \bar{v}_t = \frac{v_t + v_{t-1} + \mathbf{L} v_{t-(n-1)}}{n} \quad \mathbf{n=7} \quad (7)$$

180 ESF model: the speeds are as follows.

$$181 \quad \bar{v}_t = \beta v_t + (1 - \beta) \cdot \bar{v}_{t-1} \quad (8)$$

182 The selection rules of the smoothing factor are as follows: The smoothing factor determines the
183 smoothing level and the response speed to the difference between the predicted value and the actual result.

184 The situation of the time series model of velocity multiplicative inverse element should be as stable and
185 regular as possible, and the influence of the forward actual value on the fast smooth response degree and
186 the slow smooth response degree of the predicted value should be avoided to the greatest extent, hence,
187 the selection of smoothing factor $\beta=0.5$ is more appropriate.

188 This work draws on the noise reduction principle of monitoring equipment of the slope, respectively, to
189 build the short-term noise reduction model ($n=3$ day) and long-term noise model ($n=7$ day). While
190 satisfying the self-consistency of the stationarity and ergodicity in the time series model, the data
191 collected are processed in accordance with this rule. At the same time, the maximum predictive benefit
192 in predicting landslide accuracy is guaranteed when the velocity multiplication inverse velocity model is
193 used again.

194 In addition, the landslide occurrence time can be further classified by using the landslide time prediction
195 model based on gradient rate of change and the IVM model, which is mainly used to test the accuracy of

196 the landslide time prediction model of time series using IVM model. In Fig. 7, a landslide time prediction
197 model based on gradient rate of change is presented, and the concepts of safety and non-safety are
198 expounded. T_f represents the actual time of slope instability. T_{fp} represents the predicted time of slope
199 instability, and t_m represents the time when the slope enters the acceleration stage. The Y-axis represents
200 the expected excitation value of the predicted landslide, i.e., $t_m (T_{fp}-t_m)$. The curve AB represents the true
201 expectation of motivation. If the T_{fp} at time t happens to fall on the real excitation expectation line, then
202 the predicted slope instability time T_{fp} is equal to the actual slope instability time T_f . If T_{fp} at time t falls
203 just above the true expectation line, then the prediction result is not safe. That is, the T_{fp} is greater than
204 the T_f , indicating that the slope instability occurs before the predicted slope instability time T_{fp} , resulting
205 in the site construction personnel and equipment cannot be evacuated and transferred in a timely manner.
206 On the contrary, if T_{fp} falls in the triangular regional OAB, then the predicted results of the constructed
207 model are safe, which allows the timely evacuation of equipment and personnel and the implementation
208 of emergency plans before slope failure. The flowchart of landslide failure time prediction is shown in
209 Fig. 8.

210

211 3.2 Time forecast method and evaluation indexes selection of landslide

212 Ground-based Synthetic Aperture Radar is used to monitor the deformation characteristics of the
213 landslide, and its monitoring technology principle is shown in Fig. 8. Several distometric bases were put
214 in place along the perimetral and recorded cumulative displacements since January 1, 2013. Both
215 measuring points were distributed near the tangential crack outcropping along the top, and the monitoring
216 period was 1 January 2013 to April 17, 2013. Because the landslide is sudden type landslide, the
217 characteristics of its velocity curve are quite different from the general three-stage evolution law of

218 landslides. The initial period of constant velocity deformation is more lasting, and the curve morphology
219 changes slowly. In other words, the landslide will remain relatively stable for a long time before the
220 landslide, and there is no obvious macroscopic deformation sign. Instability failure can only occur when
221 the landslide enters the critical kinetic failure stage. This makes Saito M's empirical prediction model
222 limited, hence, it is necessary to seek for a more appropriate landslide time prediction model. The method
223 adopted in this model is to select speed data for testing. Normally, in the process of slope acceleration,
224 velocity, acceleration and displacement are three signals that represent the change of slope. According to
225 previous research results, in the process of the dynamic evolution of landslide, especially near the slide
226 acceleration as there will be a lag time than speed (Fig. 9), so the acceleration behavior may not be
227 directly cause the deformation of slope failure factors. At the same time, displacement cannot describe
228 the change process of slope on time scale, therefore, velocity data testing model is more suitable for this
229 model.

230

231 3.3 Selection method of Point OOA

232 The first stage is defined from the beginning of the data collection point to the end of the initial
233 attenuation stage. The authors select the OOA point according to the reference from the method proposed
234 by Dick et al. 2015. From the initial attenuation stage (regression phase), the newly collected data is
235 continuously fitted and modified until it approaches the value of 0. That is, it can give the prediction
236 decision for the landslide disaster prevention and control. The first stage of hierarchical early warning
237 signals is divided into point OOA and point End of Acceleration (EOA). When the Point OOA is detected,
238 the secondary attenuation stage (progressive stage) is found, and the linear recursive phase fitting
239 calculation is performed from the trend point (TP). If the regression and progressive stages are not clearly

240 divided, it can be understood as the point End of Acceleration (EOA), and the security signal is returned.

241 In this work, four smooth transition submodels of IVM are introduced, and the identification of OOA

242 point needs to be based on the linear fitting accuracy from this point to the predicted landslide period.

243

244 **4. Analysis of forecast time of the open-pit mine landslide**

245 4.1 Performance of the model under the action of weak noise

246 Displacement data were extracted from the measuring points 515-3300, and the velocity raw data and

247 displacement accumulation were shown in Fig. 10a. Landslide time prediction of time series of velocity

248 data of measuring point 515-3300 using IVM models are shown in Fig. 11a. Figs. 10b and 10c show that,

249 when the landslide does not enter the acceleration stage, the velocity data after transformation shows a

250 corrugated type and fluctuates up and down in a certain range. This model can detect speed outliers

251 caused by instrumental noise and the environmental noise. However, when the landslide enters the

252 acceleration starting stage, the velocity data after transformation gradually attenuates to zero and shows

253 a linear expression of uniform trend distribution.

254 The landslide acceleration starting point (Trend Point) of the landslide is fitted linearly. The general

255 global optimization algorithm is adopted in the fitting process. The method has the characteristic of

256 independent of the initial value, and the calculation speed is faster and the solving precision is higher in

257 the process of landslide time prediction fitting using IVM. The analysis process of each model is as

258 follows.

259 (a) Raw data model

260 Take the measuring point 515-3300 with a large displacement variation as an example, the transformation

261 results of raw data model is as shown in Fig. 11a. Fig. 10a shows that stage of 2013/01/01-2013/02/20

262 has a large fluctuation, indicating that this stage is the initial attenuation stage (Regressive Stage). After
263 2013/02/20, the amplitude enters a relatively stable phase of further attenuation (Progressive Stage). The
264 amplitude of oscillation in this stage is lower than that in the initial attenuation stage. Since 2013/04/01,
265 the curve shows obvious linear characteristics. Fig. 11a shows that the predicted landslide time under the
266 model is about 0.4 days earlier than the actual landslide time (i.e. $\Delta T=0.4$ Day), and the predicted time
267 is basically consistent with each other, basically satisfying the predicted effect.

268 (b) SSF model

269 the transformation results of SSF model is as shown in Fig. 11b. Fig. 11b shows that in the stage
270 2013/01/01-2013/02/17, the amplitude of oscillation is relatively large, which indicates that this stage is
271 the initial attenuation stage of the SSF model. The time for the displacement in under the SSF model, the
272 time for the displacement to decay significantly and enter into a relatively stable decay phase was about
273 three days earlier than that under the model with source velocity data. Through the comparison with the
274 raw data and SSF model, the velocity data processed by SSF has good connectivity between the initial
275 attenuation stage and the second attenuation stage, and the amplitude uniformity is relatively consistent.
276 Since 2013/04/02, the slope has entered a significant linear change stage, that is, the slope has entered an
277 acceleration stage. It can be seen from the curve characteristics that the SSF model, based on the raw
278 data model, makes the ladder shape of the curve have an obvious tendency to eliminate, and the prediction
279 effect is about 0.4 days in advance ($\Delta T=0.4$ Day) (Fig. 11b). The prediction effect of SSF model is to
280 make advance prediction before the actual time of landslide.

281 (c) LSF model

282 The transformation results of LSF model is shown in Fig. 11c. In phase of 2013/01/01-2013/02/26, the
283 oscillation amplitude of the measured point data is relatively large, which is also the initial attenuation

284 phase of the LSF model. The displacement in the LSF model attenuates significantly and enters a
285 relatively stable attenuating phase, which are 6 and 11 days later than the Raw data model and the LSF
286 model, respectively. The fluctuation boundary between the regressive stage and the progressive stage is
287 also obvious. Under the LSF model, the curve shows that the slope has entered an obvious linear
288 expression stage since 2013/04/05, which indicates that the slope has entered an acceleration stage. In
289 terms of curve shape, LSF model presents a better fitting state based on raw Data model and SSF model
290 respectively, but the landslide prediction time lags about 2.1 days (i.e. $\Delta T = -2.1$ Day) (Fig. 10c).

291 (d) ESF model

292 The transformation results of ESF model is shown in Fig. 11d. The phase of 2013/01/01-2013/02/26 is
293 the regressive stage of ESF model. In the ESF model, the time to enter the relatively stable attenuation
294 phase with a large displacement attenuation, which is 6 and 11 days later than that in the Raw data and
295 SSF models, respectively, which is the same as in the LSF model. Under this ESF model, the curve shows
296 that the slope has entered a significant linear change stage since 2013/04/05, that is, the slope has entered
297 an acceleration stage. In terms of curve shape, compared with Raw data model, SSF Model and LSF
298 model, the ESF Model has the lowest fitting accuracy, with a linear fitting correlation coefficient of only
299 0.86, but the predicted landslide time is consistent with the reality (i.e., $\Delta T = Ta$) (Fig. 11d).

300 Fig. 12 shows the slope life expectancy curve under the four models. Except the ESF model, the curve
301 morphology of the other models is approximate to the actual life expectancy time line in the slope failure
302 process and converges in parallel. Fig. 12b shows that from 2013/04/10, the expected life expectancy
303 curve of the slope is approximately the same as the actual life expectancy curve after the slope enters the
304 acceleration stage. Fig. 12c shows that the slope life expectancy curve under LSF model intersects with
305 the actual slope life expectancy curve in 2020/04/05, and finally deviates from the actual landslide time,

306 presenting a delayed predictive expression effect. This indicates that the final prediction results show
307 signs of lag outside the security range, and also verifies the accuracy of the fitting calculation results of
308 LSF model. The slope life expectancy under ESF model is similar to the actual time, but compared with
309 Raw data, SSF and LSF models, the slope life expectancy correlation curve has no obvious regularity.

310

311 4.2 Performance of the model under the action of strong noise

312 Landslide time prediction of time series of velocity data of measuring point 461-3250 using IVM is
313 shown in Fig. 13. In the four models, the fluctuation and amplitude of the curve are large in the
314 regressive stage. This is because the overlying strata in the goaf are disturbed by well mining near
315 the open-pit mine landslide, and the slope is also disturbed by the open-pit mining cycle. The above
316 two kinds of perturbations make the inverse velocity characteristic curve show obvious fluctuation
317 characteristics. To explore the applicability of the IVM time prediction model of landslide under
318 strong noise, the measuring point 461-3250 is taken as an example to test the model. The
319 representation features of the four models are shown in Fig. 13, and the specific analysis process is
320 as follows.

321 (a) Raw data model

322 Fig. 13a shows that the regressive stage is 2013/1/01-2013/2/22. The progressive stage is 2013/2/22-
323 2013/4/4. It is noteworthy that the curve shape of the source velocity data presents a slightly concave
324 shape from 2020/4/01 to 2020/4/11 (Fig. 13a). This is because of noise (disturbance of mining,
325 disturbance of adjacent well construction, natural factors, etc.), resulting in no uniform change during
326 the acceleration stage of the landslide. At the same time, although the landslide time prediction was
327 brought forward by about 4.8 days ($\Delta T=4.8$ Day), as shown in Fig.13a, since the slope data acquisition

328 frequency unit of the open-pit mine is "day", the prediction value of landslide risk evaluation and
329 anticipation of disaster prevention decision have to be too futuristic. This may cause economic loss to
330 open-pit mine, so there is no clear guiding significance for the disaster prevention and mitigation of open-
331 pit mine landslide.

332 (b) SSF model

333 The data after the inverse velocity transformation using SSF model is shown in [Fig. 13b](#). [Fig. 13b](#) shows
334 that the regressive stage of the landslide evolution process was 2013/1/01-2013/2/23. The progressive
335 stage is 2013/2/23-2013/4/4. Although fluctuation amplitude decreased in Regressive stage (with a range
336 of 0~1.5day/mm), its oscillating patterns did not change significantly with SSF model treatment. In
337 regressive stage, fluctuation shapes still showed an irregular trend. The specific performance was
338 concentrated in the periods of 2013/01/06-2013/01/09, 2013/01/29-2013/02/05 and 2013/02/12-
339 2013/02/19. It can be speculated that the fluctuation in this period is mainly influenced by Environment
340 Noise. After the landslide enters the acceleration stage (namely the linear regression stage), the inverse
341 velocity data processed by SSF model does not show good fitting ability.

342 (c) LSF model

343 The velocity raw data transformed by LSF model is shown in [Fig. 13c](#). The period of 2013/01/01-
344 2013/02/26 is the regressive stage. Compared with raw data and SSF models, the inverse velocity curve
345 is smoother after using LSF model. In LSF model, the curve shows that the slope has entered a more
346 significant linear regression stage since 2013/04/06, that is, the slope has entered an acceleration stage.
347 Compared with the stepped curves of acceleration stage in [Figs. 13a, b, c](#) shows some degree of
348 weakening and good smoothness. The landslide prediction time result obtained by using the LSF model
349 is about 0.2 days before the actual landslide occurrence time ($\Delta T=0.2$ Day) ([Fig. 13c](#)), which is more in

350 line with the actual situation and has good prediction effect, and can be used as the decision reference
351 for landslide prevention.

352 (d) ESF model

353 The inverse velocity curve of velocity raw data using ESF model is shown in Fig. 13d. The period of
354 2013/01/01-2013/02/26 is the regressive stage. The ESF model is similar to the regressive stage in the
355 Raw data model. Although the amplitude of ESF model is large (0-1.4 day/mm), its smoothness is not
356 well improved. Fig. 13d shows that ESF model is similar to LSF model, however, due to the smoothness
357 of regressive smoothness and overall fitting of progressive stage is not ideal, therefore, the prediction
358 performance of ESF model for noisy velocity data needs to be further improved.

359 The slope life expectancy curves of the four models are shown in Fig. 14. During 2013/04/01-2013/04/03,
360 the slope life expectancy curve predicted by SSF and LSF models was approximately parallel to the
361 actual life expectancy curve. Since 2013/04/09, that is, about one week before the actual occurrence of
362 the landslide, the slope life expectancy curve of the prediction model using SSF and LSF models and the
363 actual slope life expectancy curve have been approximately parallel convergence and coincidence
364 convergence respectively. However, there is no coincidence between the prediction signal effect and the
365 actual slope life expectancy curve in the end. The slope life expectancy curve predicted by ESF model
366 intersects with the actual slope life expectancy curve on 2013/04/05/and 2013/04/11, and the predicted
367 landslide time is not within the safe range. Compared with SSF, LSF and ESF models, the parallel
368 convergence characteristics of the curves in the early stage of the acceleration phase of LSF model
369 (2013/04/01-2013/04/10 period) are relatively regular. The predicted slope life expectancy curve and the
370 actual slope life expectancy curve approximately produce a form of parallel convergence on 2013/04/10,
371 and the two curves completely coincide on 2013/04/15, which also verifies the advance prediction result

372 fitted by LSF model in the Progressive stage. Therefore, the prediction accuracy of LSF model for
373 measuring points with high noise is relatively high.

374

375 4.3 Performance of scale model with different displacement variation

376 To explore the performance of the four models for landslide prediction at small velocity changes and the
377 sensitivity identification of slopes at different stages of landslides evolution. Taking the measuring points
378 548-2200 and 461-3250 with small change of displacement as examples, the application analysis of the
379 model is carried out. The velocity variation of the two points is shown in Fig. 15. Because the landslide
380 is characterized by a sudden, the displacement change in the early stage of the landslide is not obvious,
381 but when the landslide is about to happen, the displacement shows a sudden increase. To clearly analyze
382 the difference between the two measurement points, the velocity curve during the accelerated start-up
383 period was enlarged (Fig. 15). The corresponding variation range of measuring points 548-2200 and 461-
384 3250 was 0-50 mm/day and 0-240 mm/day, respectively. In the acceleration starting stage of the landslide,
385 the velocity curve of the measured point 461-3250 shows an exponential trend, which indicates that the
386 landslide bursting characteristics are more obvious. The velocity curve of measuring point 548-2200
387 presents a stepped form.

388 The inverse velocity curve of the measured point 548-2200 using the raw data model is shown in Fig.
389 16a. From 2013/01/01 to 2013/03/29, regressive stage was used as the initial decay stage. With a
390 relatively high rate of displacement change, the regressive stage lagged behind for about a month when
391 compared with measurement point 461-3250. Since 2013/03/29, the inverse velocity curve entered the
392 progressive stage with a reduced amplitude and a short duration. Since 2013/04/14, it has entered the
393 stage of linear regression (i.e. the stage of continuous acceleration). Fig. 16a shows that although the

394 predicted landslide time obtained using Raw Data model is 1.1 days earlier than the true time ($\Delta T=1.1$
395 Day). However, Fig. 16a shows that the prediction results of landslide time are not reliable because the
396 correlation coefficient of curve fitting is 0.81 and the determination coefficient is 0.78. Based on the
397 above analysis of the measured point 548-2200 with small displacement variation, in the reciprocal
398 representation method of time series velocity data. Fig. 16a shows that the initial regression stage of the
399 measuring point 548-2200 has a longer time period, and the second decay stage and the linear regression
400 stage define a shorter time period, in particular, the 2013/04/14-2013/04/17 is the linear recursion phase.
401 This indicates that there are few data used to fit and solve landslide prediction time. Even if the prediction
402 results are shown to be in advance, the verification results have a large error with the actual ones, and
403 are not applicable to the open-pit mine.

404 (b) SSF model

405 Fig. 16b shows the inverse velocity curve after SSF model transformation. 2013/01/01-2013/03/31 is the
406 Regressive Stage. Compared with raw data model, the time for SSF model to enter the progressive stage
407 lags about two days. Since 2013/04/09, the slope has entered an obvious linear expression stage, which
408 indicates that the slope has entered an acceleration stage. From the curve shape (Fig. 16b), the local
409 fitting performance of SSF model for the accelerated curve is not ideal, which is similar to the analysis
410 result using raw data model. The landslide prediction time is about 1.2 days in advance ($\Delta T=1.2$ Day),
411 and it has no guiding significance for landslide prediction.

412 (c) LSF model

413 Fig. 16c shows the inverse velocity curve using LSF model transformation. It can be found that the
414 critical time between regressive stage and progressive stage is 2013/03/30, which lags about one day
415 using SSF model. The fitting results of LSF model is shown in Fig. 16c. The correlation coefficient and

416 determination coefficient of curve fitting are 0.96 and 0.78, respectively. The prediction time of LSF
417 model is 0.2 days earlier ($\Delta T=0.2$ Day), which is close to the actual landslide time and more in line with
418 the actual situation. Therefore, for the measuring points with small displacement variation, the fitting
419 accuracy and predicted time performance of the LSF model are better and more in line with the reality.

420 (d) ESF model

421 The inverse velocity curve after EFS model transformation is shown in Fig. 16d. The prediction results
422 of ESF model and LSF model are similar, and its prediction time is 0.4 days earlier ($\Delta T=0.4$ Day).

423 Combined with the measuring point 548-2200 with a small displacement change and the point 461-3250
424 with a large displacement change, the landslide time prediction results of the two points were compared:

425 When the displacement change is small, the prediction effect of the model on the boundary point between
426 the initial regression stage and the second decay stage is not perfect, and there is a hysteresis effect. The
427 raw data and SSF models were not ideal for the landslide acceleration phase when the four models were
428 used for smooth transition. The applicability of the four models can be summarized as follows: when the
429 velocity changes greatly, LSF model is recommended for landslide time prediction, while for short-term
430 irregular data, while ESF model is recommended for landslide time prediction after data preprocessing.

431 The accuracy and rationality of the calculated results are compared between the predicted and actual
432 slope life expectancy. The predicted slope life expectancy curves of the four models and the actual slope
433 life expectancy curves are shown in Figs. 17a-c shows that in the raw data model, the two curves show
434 a parallel convergence trend since 2013/04/13, and the predicted slope life expectancy curve is about 0.8
435 days earlier than the landslide ($\Delta T=0.8$ Day), which is almost consistent with the fitting result (Fig. 17a).

436 However, this prediction result is seldom used in training fitting data, and its verification results are
437 difficult to be used as a reference for prediction. In SSF model, since 2013/04/10, the curves of the

438 prediction model and the actual model converge approximately in parallel, which adds to the
439 phenomenon of time lag in landslide prediction (Fig. 17b). In the LSF model, the curve has a special
440 shape. Since 2013/04/06, the predicted life expectancy point of the slope is above the actual expected
441 curve of the slope, and is defined as the danger range. In the period of 2013/04/07-2013/04/08, the line
442 between the two expectation points in this stage is approximately parallel to the convergence of the actual
443 slope life expectancy curve, but it is also above the actual slope expectation curve and is still defined as
444 within the danger range.

445

446 **5. Discussion: Grading forecast of inverse velocity expression**

447 The landslide time prediction model based on IVM mainly determines the acceleration starting point
448 (Trend Point) of landslide by transforming the slope velocity data, and then predicts the landslide time
449 in the linear recursive stage. This method has the following advantages in combination with the open-pit
450 mine landslide. For the original velocity data with obvious curve shape boundary, this method can be
451 used to predict the landslide time, and the prediction accuracy and the fitting effect of linear regression
452 stage are self-consistent. For sudden type landslides with large data noise, the moment of the initial
453 acceleration stage of the landslide can be captured. The reliability of the models is affected by noise, and
454 the application of SSF and LSF models is not clearly defined. The following is a comparative analysis
455 of the applicability of the two models in the hierarchical prediction of inverse velocity expression.

456

457 5.1 First order prediction

458 Based on the above analysis, the LSF model has the defect of delayed prediction, while the SFF model
459 is not sensitive enough to the noise change of velocity data. To avoid the shortcomings of the two models

460 and give full play to their respective advantages in landslide time prediction, the expression mode of
461 parallel intersection of the models was used to discuss. Specific methods and steps are as follows.

462 Combined with the monitoring data of LSF and SSF models, an example of measuring point 515-3300
463 was taken for analysis. The displacement variation and data form of the measuring point show great noise.
464 The intersection between a short - and long - term smooth movement is usually one of the most basic
465 signals that indicate a trend change in the source velocity data. The speed curve processed by SSF model
466 (gray curve) and LSF model (red curve) is shown in Fig. 18. The two curves show a cross shape. Based
467 on the performance of long-term and short-term smooth prediction, the following assumptions are
468 proposed: When the SSF model curve is interlaced with the LSF model curve at one point, after crossing
469 the Crossover point, if the SSF model curve is on the LSF model curve, the time period is defined as the
470 positive Crossover interval, namely, the positive Crossover point. Conversely, it is defined as a negative
471 intersection.

472 Based on the above analysis, the long-term and short-term velocity data of monitoring point 515-3300
473 are analyzed. Taking 3 days as the time unit of short-term smooth transition, the velocity data is processed
474 by short-term moving average. Taking 14 days as the time unit of long-term smooth transition, the long-
475 term moving smooth filtering is performed on the velocity data. There is no standard range for the time
476 interval of long-term and short-term smoothing. Different range of long-term and short-term smoothing
477 will have different effects on the actual analysis and prediction results. According to the actual situation
478 of the landslide (such as the acquisition frequency and displacement change rate of the monitoring
479 equipment affected by mining disturbance, high noise level and other factors), the 3-day and 14-day
480 moving period is more in line with the actual situation, and can make the short-term and long-term
481 differences more obvious. The SSF model curve crossed with the SSF model curve for the first time on

482 March 29, 2013; then, the two model curves showed an obvious downward trend, crossed for the second
483 time on March 22, 2013, and then showed an upward trend in an approximate fitting shape; Combined
484 with the actual situation, the second cross slope does not show obvious change, so the second cross point
485 is regarded as the end point of the first acceleration. April 1, 2013 is the second intersection, which is the
486 same as trend point (Fig. 18a).

487 Therefore, the analysis of the parallel use of SSF and LSF models has the following advantages: In the
488 process of monitoring, when the two are positively crossed, the first threshold can automatically send
489 signals. To some extent, it avoided the subjectivity of determining different observation points by
490 experience, and increased the standardization of judgment of point OOA. If this method is applied to the
491 radar monitoring of open-pit mines, it can theoretically provide reference for the dynamic evaluation of
492 displacement change rate of multiple measurement points at the same time. It can then be extended to
493 the risk assessment of landslide hazards, and the magnitude of regional instability can be estimated
494 through multiple monitoring points distributed on a spatial scale. Finally, the identification signal of the
495 acceleration phase is used to determine whether it is the local acceleration motion performance or the
496 acceleration of all measuring points.

497

498 5.2 Second order prediction

499 To improve the reliability of the method in predicting landslide instability, the SSF and LSF models were
500 used to transform the data suitable for the inverse velocity model in the first stage to obtain the best
501 fitting curve. Since the prediction performance of the SSF and LSF models is different, they will get
502 different landslide prediction time, and the difference between them is expressed as Δ . The time scale
503 predicted by the two models is assumed, namely, $T_{f(SSF)} < T_{f(LMA)}$; The window interval of landslide

504 instability can be expressed as:

$$505 \quad [T_{f(SMA)} - \frac{\Delta}{2}; T_{f(LMA)} + \frac{\Delta}{2}] \quad (9)$$

506 In the prediction model, when the required test time $T > T_{f(SMA)} - \Delta/2$ corresponds to the second-level
507 activation cycle of landslide time prediction alarm. However, there are no clear rules for determining the
508 limit value of the windowing parameter T_{fw} using the established parameter Δ ; These parameters should
509 be set according to the specific engineering application. In addition, in order to make the time covered
510 by T_{fw} long enough to consider the uncertainty in landslide time prediction, the boundary of detection
511 failure time window should be widened, and the edge of the perimeter area is defined as $\Delta/2$ at the same
512 time. In particular, it avoids the inaccuracy of sending out the prediction signal in advance due to the
513 premature activation of the second level prediction warning threshold. In the definition of T_{fw} , the
514 assessment of landslide disaster risk factors and the specific characteristics of landslide emergency plan
515 should also be considered. The grading prediction curve of the measuring point 515-3300 with low noise
516 is shown in Fig. 18a. The model established a 5-day "time window" in 2013/04/15-2013/04/20. The
517 actual landslide time was at 1/3 of the interval $T_{f(SSP)} - T_{f(LMA)}$, which was located in the defined slope
518 failure window. Slope failure "windowing" should be updated with collected data. By this method, the
519 trigger time of landslide can be identified to a certain extent and the relevant decision plan can be adopted.

520

521 **6. Conclusions**

522 The landslide prediction model, method and application of open pit coal mine are studied, and some
523 conclusions are obtained as follows.

524 1. The IVM is used to investigate the early warning and prediction of open-pit landslide, and the criterion
525 of landslide instability is proposed. The IVM can be used as an effective tool to predict the landslide time,

526 and the influence of other exogenous factors such as region, location and material properties on the model
527 can be ignored in the prediction process. Based on the analysis results of the IVM and the kinematics
528 characteristics of the landslide, the sliding deformation evolution process of the landslide is divided into
529 three stages: the regressive stage, the progressive stage, and the autoregressive stage, that is, the initial
530 deformation stage, accelerated deformation stage, and sliding instability stage. After the inverse velocity
531 model is used to process the data, when the inverse velocity value continuously approaches 0, it can be
532 regarded as the predicted value of the occurrence time of landslide.

533 2. The accuracy of inverse velocity model prediction is closely related to the measured noise of the
534 monitoring equipment and the natural noise of the environment. Two kinds of noise data may affect the
535 inverse velocity model's recognition of different deformation stages. The four models of IVM are
536 proposed to solve the above problem, including the raw data, SSF, LSF, and ESF models. The
537 applicability of the four models in the early warning and prediction of open-pit mine landslide is
538 compared and analyzed. Compared with Raw data and ESF models, the fitting effect of SSF and LSF
539 was better when entering the linear autoregressive stage. By analyzing the inverse velocity curve shape,
540 SSF and LSF models have different prediction performance.

541 3. OOA point is very important in IVM for landslide early warning and prediction, which is the boundary
542 point to distinguish Regressive Stage and Progressive Stage. A slope displacement pixel difference
543 method based on fitting accuracy and field monitoring signals is proposed to determine the point 00A.
544 On this basis, a hierarchical prediction method was proposed. The cut-off point of autoregressive stage
545 in the inverse velocity model was used as the identification point of the first-level warning threshold, and
546 was further defined by analyzing the intersection points of SSF and LSF. The second level demarcation
547 point is defined by adding failure window.

548

549 **Author contribution**

550 Han Du performed the data analyses and wrote the manuscript; Danqing Song helped perform the
551 analysis with constructive discussions; Weiqiang Guo, Lihu Dong and Yukai Wang carried out
552 subsequent field investigations.

553

554 **Declaration of competing interest**

555 The authors declare that they have no known competing financial interests or personal relationships that
556 could have appeared to influence the work reported in this paper.

557

558 **Acknowledgments**

559 This study was supported by the China Postdoctoral Science Foundation (2020M680583), the National
560 Postdoctoral Program for Innovative Talent of China (BX20200191), the Excellent Sino-foreign Youth
561 Exchange Program of China Association for Science and Technology in 2020 (No. 58), and the Shuimu
562 Tsinghua Scholar Program (2019SM058).

563

564 **References**

- 565 Admassu, Y., Shakoor, A., Wells, N.A., 2012. Evaluating selected factors affecting the depth of
566 undercutting in rocks subject to differential weathering. Eng. Geol. 124, 1–11.
567 <https://doi.org/10.1016/j.enggeo.2011.09.007>
- 568 Bozzano, F., Cipriani, I., Mazzanti, P., Prestininzi, A., 2014. A field experiment for calibrating landslide
569 time-of-failure prediction functions. Int. J. Rock Mech. Min. Sci. 67, 69–77.

570 Bozzano, F., Mazzanti, P., Prestininzi, A., Mugnozza, G.S, 2010. Research and development of advanced
571 technologies for landslide hazard analysis in Italy. *Landslides*. 7 (3), 381-385. [https://doi.org](https://doi.org/10.1007/s10346-010-0208-x/)
572 [10.1007/s10346-010-0208-x/](https://doi.org/10.1007/s10346-010-0208-x/)

573 Carlà, T., Intrieri, E., Di Traglia, F., Nolesini, T., Gigli, G., Casagli, N., 2017. Guidelines on the use of
574 inverse velocity method as a tool for setting alarm thresholds and forecasting landslides and structure
575 collapses. *Landslides*. 14(2), 517–534. <https://doi.org/10.1007/s10346-016-0731-5>

576 Chen Z, Song, DQ, Hu C, Ke YT (2020) The September 16, 2017, Linjiabang landslide in Wanyuan
577 County, China: preliminary investigation and emergency mitigation. *Landslides* 17(1):191–204.
578 <https://doi.org/10.1007/s10346-019-01309-1>

579 Chen, M.X., Jiang, Q.H., 2020. An early warning system integrating time-of-failure analysis and alert
580 procedure for slope failures. *Eng. Geol.* 272, 105629. <https://doi.org/10.1016/j.enggeo.2020.105629>

581 Chen, Z., Song, D.Q., 2021. Numerical investigation of the recent Chenhecun landslide (Gansu, China)
582 using the discrete element method. *Nat. Hazards*. 105(1), 717–733. [https://doi.org/10.1007/s11069-020-](https://doi.org/10.1007/s11069-020-04333-w)
583 [04333-w](https://doi.org/10.1007/s11069-020-04333-w)

584 Dick, G.J., Eberhardt, E., Cabrejo-Liévano, A.G., Stead, D., Rose, N.D., 2015. Development of an early-
585 warning time-of-failure analysis methodology for open-pit mine slopes utilizing ground-based slope
586 stability radar monitoring data. *Can. Geotech. J.* 52(4), 515-529. <https://doi.org/10.1139/cgj-2014-0028>

587 Du, H., Song, D., Chen, Z., Shu, H., Guo, Z.Z., 2020. Prediction model oriented for landslide
588 displacement with step-like curve by applying ensemble empirical mode decomposition and the PSO-
589 ELM method. *J. Clean Prod.* 270:122248. <https://doi.org/10.1016/j.jclepro.2020.122248>

590 Fan, X.M., Domenech, G., Scaringi, G., Huang, R.Q., Xu, Q., Hales, T., Dai, L.X., Yang, Q., Francis, O.,
591 2018. *Landslides*. 15(12), 2325-2341. <https://doi.org/10.1007/s10346-018-1054-5>

592 Fukuzono, T., 1985. A new method for predicting the failure time of slopes. In: Japan Landslide Society
593 Committee for International Exchange of Landslide Technique (ed) Proceedings of 4th International
594 Conference and Field Workshop on Landslides, Tokyo, Japan, 23-31 August, pp 145–150.

595 Gao, Y., Yin Y.P., Li, B., Feng, Z., Wang, W.P., Zhang, N., Xing, A.G., 2017. Characteristics and
596 numerical runout modeling of the heavy rainfall-induced catastrophic landslide–debris flow at Sanxicun,
597 Dujiangyan, China, following the Wenchuan MS 8.0 earthquake. *Landslides*. 14(4)1361–1374.
598 <https://doi.org/10.1007/s10346-016-0793-4>

599 Haque, U., da-Silva, P.F., Devoli, G., Pilz, J., Zhao, B.X., Khaloua, A., Wilopo, W., Andersen, P., Lu, P.,
600 Lee, J., Yamamoto, T., Keellings, D., Wu, J.H., Glass, G.E., 2019. The human cost of global warming:
601 Deadly landslides and their triggers (1995 – 2014). *Sci. Total Environ.* 682, 673 – 684. [https://doi.org/](https://doi.org/10.1016/j.scitotenv.2019.03.415)
602 [10.1016/j.scitotenv.2019.03.415](https://doi.org/10.1016/j.scitotenv.2019.03.415)

603 He, L.P., Tan, J., Hu, Q.J., He, S.S., Cai, Q.J., Fu, Y.T., Tang, S., 2018. Non-contact measurement of the
604 surface displacement of a slope based on a smart binocular vision system. *Sensors*. 18(9). 2890.
605 <https://doi.org/10.3390/s18092890>

606 Kim, D.H., Gratchev, I., Balasubramaniam, A., 2015. Back analysis of a natural jointed rock slope based
607 on the photogrammetry method. *Landslides* 12(1):147-154. <https://doi.org/10.1007/s10346-014-0528-3>

608 Liu, G.W., Song, D.Q., Chen, Z., Yang, J.W., 2020. Dynamic response characteristics and failure
609 mechanisms of coal slopes with weak intercalated layers under blasting loads. *Adv Civ Eng*. 5412795.
610 <https://doi.org/10.1155/2020/5412795>

611 López-Vinielles, J., Ezquerro, P., Fernández-Merodo, J.A., Béjar-Pizarro M., Monserrat, O., Barra, A.,
612 Blanco, P., García-Robles, J., Filatov, A., García-Davalillo, J.C., Sarro, R., Mulas, J., Mateos, R.M.,
613 Azañón, J.M., Galve, J.P., Herrera, G., 2020 Remote analysis of an open-pit slope failure: Las Cruces

614 case study, Spain. *Landslides*. 17(9), 2173-2188. <https://doi.org/10.1007/s10346-020-01413-7>

615 Luzi, G., 2010. Ground based SAR interferometry: a modified tool for geoscience. In: Imperatore, P.,
616 Riccio, D. (Eds.), *Geoscience and Remote Sensing, New Achievements*, 978-953-7619-97-8. inTech
617 Open Access Publisher, Rijeka, Croatia, pp. 1–26.

618 Ma, G.T., Hu, X.W., Yin, Y.P., Luo, G., Pan, Y.X., 2018. Failure mechanisms and development of
619 catastrophic rockslides triggered by precipitation and open-pit mining in Emei, Sichuan, China.
620 *Landslides*. 15(7), 1401–1414. <https://doi.org/10.1007/s10346-018-0981-5>

621 Mazzanti, P., 2011. Displacement monitoring by terrestrial SAR interferometry for geotechnical purposes.
622 *Geotech. Instrum. News* 29 (2), 25–28.

623 Mufundirwa, A., Fujii, Y., Kodama, J., 2010. A new practical method for prediction of geomechanical
624 failure. *Int J Rock Mech Min Sci*. 47(7), 1079 – 1090. <https://doi.org/10.1016/j.ijrmms.2010.07.001>

625 Osasan, K.S., Stacey, T.R., 2014. Automatic prediction of time to failure of open pit mine slopes based
626 on radar monitoring and inverse velocity method - sciencedirect. *Int. J. Min. Sci. Tech*. 24(2), 275-280.
627 <http://dx.doi.org/10.1016/j.ijmst.2014.01.021>

628 Rose, N.D., Hungr, O., 2007. Forecasting potential rock slope failure in open pit mines using t
629 he inverse-velocity method. *Int. J. Rock Mech. Min. Sci*. 44(2), 308-320. [https://doi.org/10.1016](https://doi.org/10.1016/j.ijrmms.2006.07.014)
630 [/j.ijrmms.2006.07.014](https://doi.org/10.1016/j.ijrmms.2006.07.014)

631 Severin, J., Eberhardt, E., Leoni, L., Fortin, S., 2014. Development and application of a pseudo-3d pit
632 slope displacement map derived from ground-based radar. *Eng. Geol.* 181, 202-211. [https://doi.org/](https://doi.org/10.1016/j.enggeo.2014.07.016)
633 [10.1016/j.enggeo.2014.07.016](https://doi.org/10.1016/j.enggeo.2014.07.016)

634 Song, D.Q., Chen, Z., Ke, Y.T., Nie, W., 2020a. Seismic response analysis of a bedding rock slope based
635 on the time-frequency joint analysis method: a case study from the middle reach of the Jinsha River,

636 China. Eng. Geol. 274, 105731. <https://doi.org/10.1016/j.enggeo.2020.105731>

637 Song, D.Q., Liu, X.L., Chen, Z., Chen, J.D., Cai, J.H., 2020b. Influence of Tunnel Excavation on the
638 Stability of a Bedded Rock Slope: A Case Study on the Mountainous Area in Southern Anhui, China.
639 KSCE J. Civ. Eng. 25(1), 114-123. <https://doi.org/10.1007/s12205-020-0831-6>

640 Song, D.Q., Liu, X.L., Huang, J., Wang, E.Z., Zhang, J.M., 2020d. Characteristics of wave propagation
641 through rock mass slopes with weak structural planes and their impacts on the seismic response
642 characteristics of slopes: a case study in the middle reaches of Jinsha River. Bull. Eng. Geol. Environ.
643 80(2), 1317-1334. <https://doi.org/10.1007/s10064-020-02008-1>

644 Song, D.Q., Liu, X.L., Huang, J., Zhang, J.M., 2020c. Energy-based analysis of seismic failure
645 mechanism of a rock slope with discontinuities using Hilbert-Huang transform and marginal spectrum
646 in the time-frequency domain. Landslides. 18(1), 1-19. <https://doi.org/10.1007/s10346-020-01491-7>

647 Song, D.Q., Liu, X.L., Li, B., Zhang, J.M., Bastos, J.J.V., 2020e. Assessing the influence of a rapid water
648 drawdown on the seismic response characteristics of a reservoir rock slope using time–frequency analysis.
649 Acta Geotech. 1-22. <https://doi.org/10.1007/s11440-020-01094-5>

650 Tarolli, P., Sofia, G., 2016. Human topographic signatures and derived geomorphic processes across
651 landscapes. Geomorphology. 255, 140-161. <https://doi.org/10.1016/j.geomorph.2015.12.007>

652 Tommaso, C., Paolo, F., Emanuele, I., Kostas, B., Nicola, C., 2017. On the monitoring and early-warning
653 of brittle slope failures in hard rock masses: examples from an open-pit mine. Eng. Geol. 228, 71 – 81.

654 Ventura, G., Vinciguerra, S., Moretti, S., Meredith, P.H., Heap, M.J., Baud, P., Shapiro, S.A., Dinske, C.,
655 Kummerow, J., 2009. Understanding slow deformation before dynamic failure. In: Tom Beer (ed)
656 Geophysical Hazards, 1st edn. Springer Netherlands, pp. 229-247.

657 Voight, B., 1989. A relation to describe rate-dependent material failure. Science 24(3),200–203.

- 658 <https://doi.org/10.1126/science.243.4888.200>
- 659 Wu, J.H., Lin, W.K., Hu, H.T., 2018. Post-failure simulations of a large slope failure using 3DEC: the
660 Hsien-du-shan slope. Eng. Geol. 242, 92-107. <https://doi.org/10.1016/j.enggeo.2018.05.018>
- 661 Zare Naghadehi, M., Jimenez, R., Khalokakaie, R., Esmail Jalali, S., 2013. A new open-pit mine slope
662 instability index defined using the improved rock engineering systems approach. Int J Rock Mech Min
663 Sci. 61,1-14. <http://dx.doi.org/10.1016/j.ijrmms.2013.01.012>
- 664 Zhou, X.P., Liu, L.J., Xu, C., 2020. A modified inverse-velocity method for predicting the failure time of
665 landslides. Eng. Geol. 268, 105521. <https://doi.org/10.1016/j.enggeo.2020.105521>

Figures

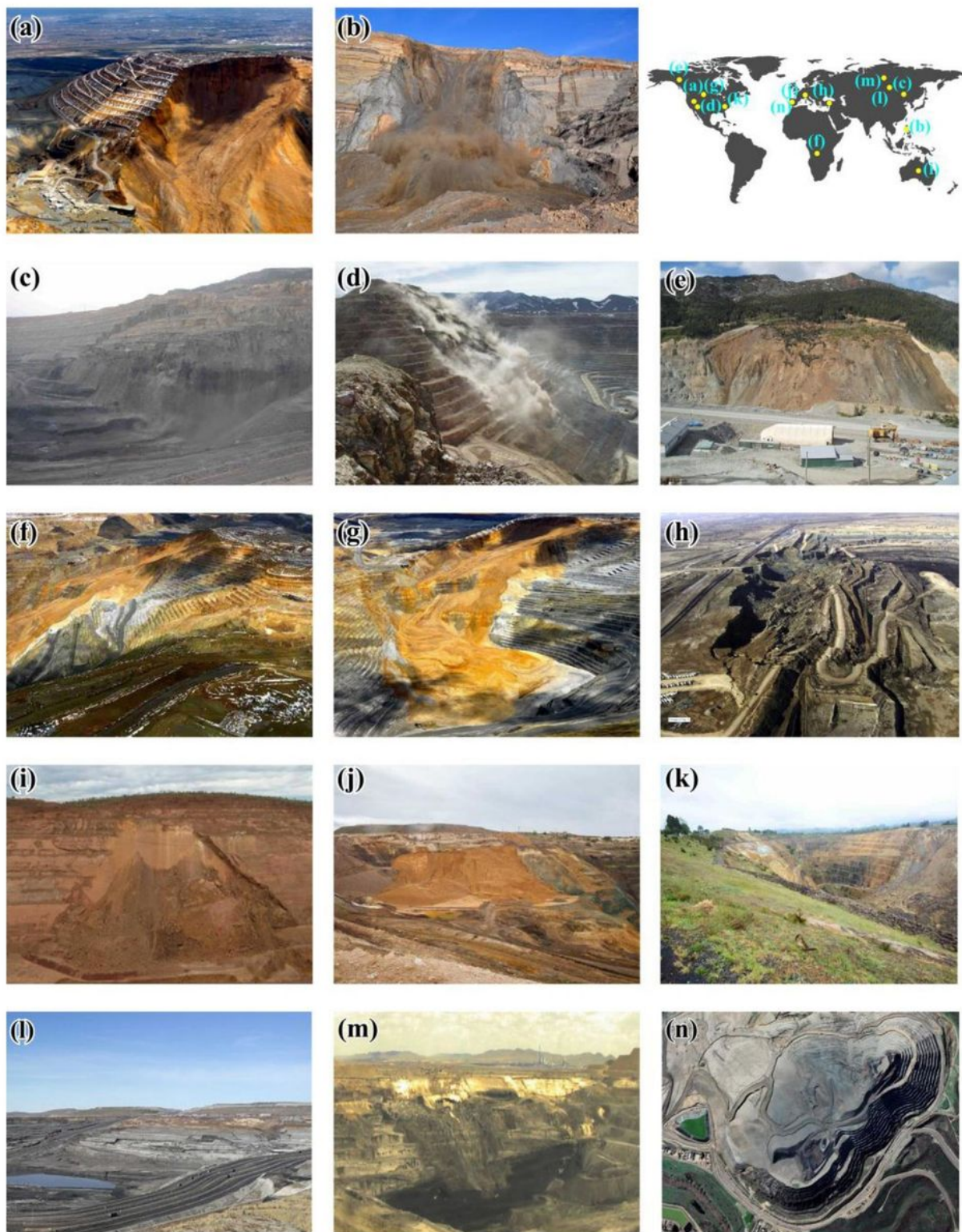


Figure 1

Worldwide surface mining landslide disastrous events from Google Retrieval and related literatures: (a) Bingham Canyon Mine, Utah, United States (Moore et al. 2016); (b) Panian Open Pit, Caluya, Philippines(<https://blogs.agu.org/landslideblog/>); (c) West Open Pit, Chifeng, China (Xiao 2014); (d)

Betze-Post Gold Mine, Nevada, United States (<https://blogs.agu.org/landslideblog/>); (e) Huckleberry Mine, Smithers British Columbia, Canada (<https://blogs.agu.org/landslideblog/>); (f) Australia; (g) Utah Copper Mine, Utah, United States (Pankow et al. 2013); (h) Çöllolar open pit mine, Elbistan Turkey (Akcar et al. 2019); (i) West Angles Centre Pit North, Australia (Venter et al. 2013); (j) Skouriotissa Mines, The Republic of Cyprus (<https://www.visitsolea.com/skouriotissa-mines/>); (k) Longwall mines, U-nited States (Behrooz 2016); (l) Baiyinhua Open Pit Mine, China (Du 2017); (m) Shengli East Open-Pit Mine, Xilinhote, China (Liu et al. 2020); (n) Las Cruces Open-pit Mine, Seville, Spain (Juan et al. 2020)

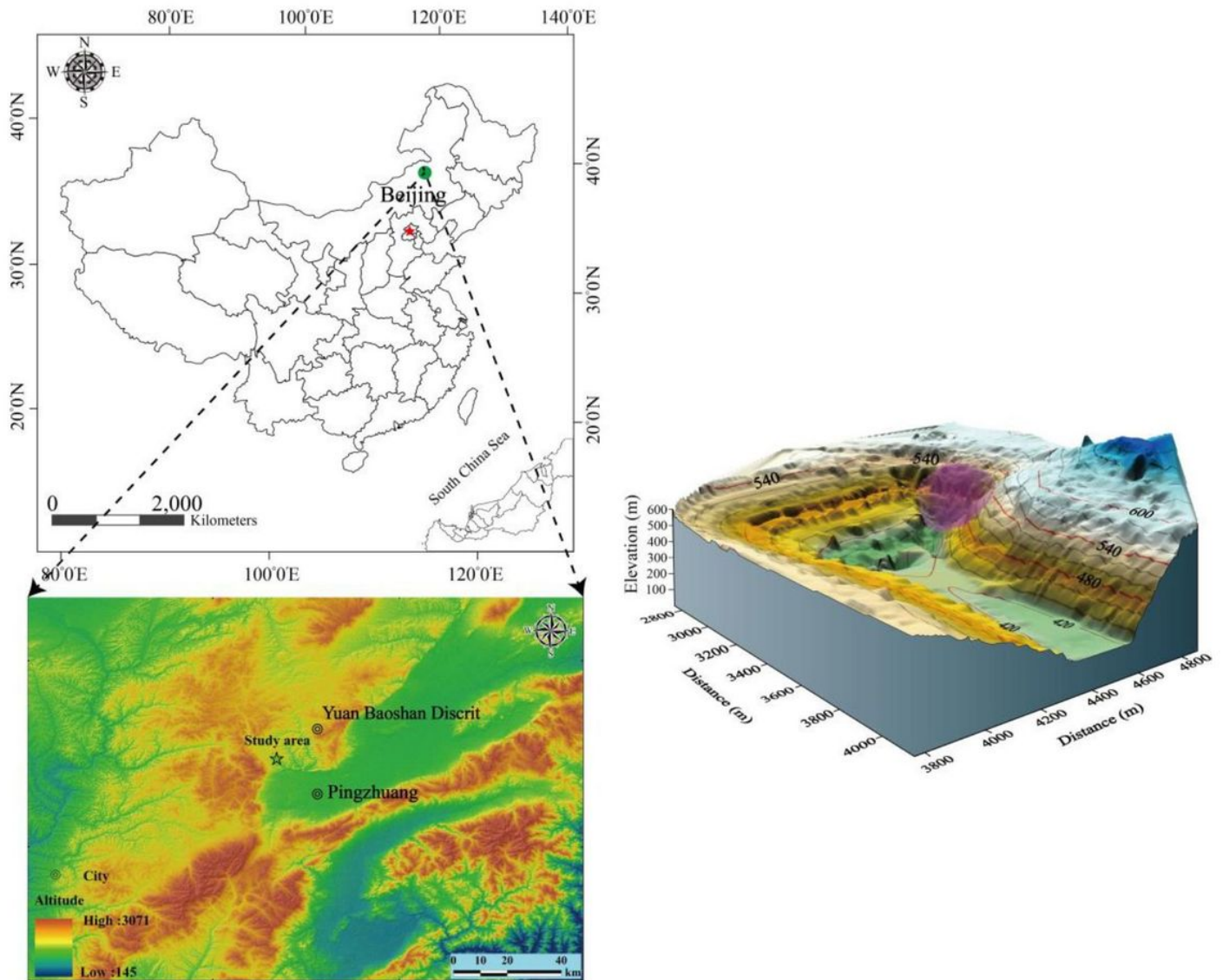


Figure 2

Location of the Pingzhuang west open-mine landslide, Inner Mongolia, China

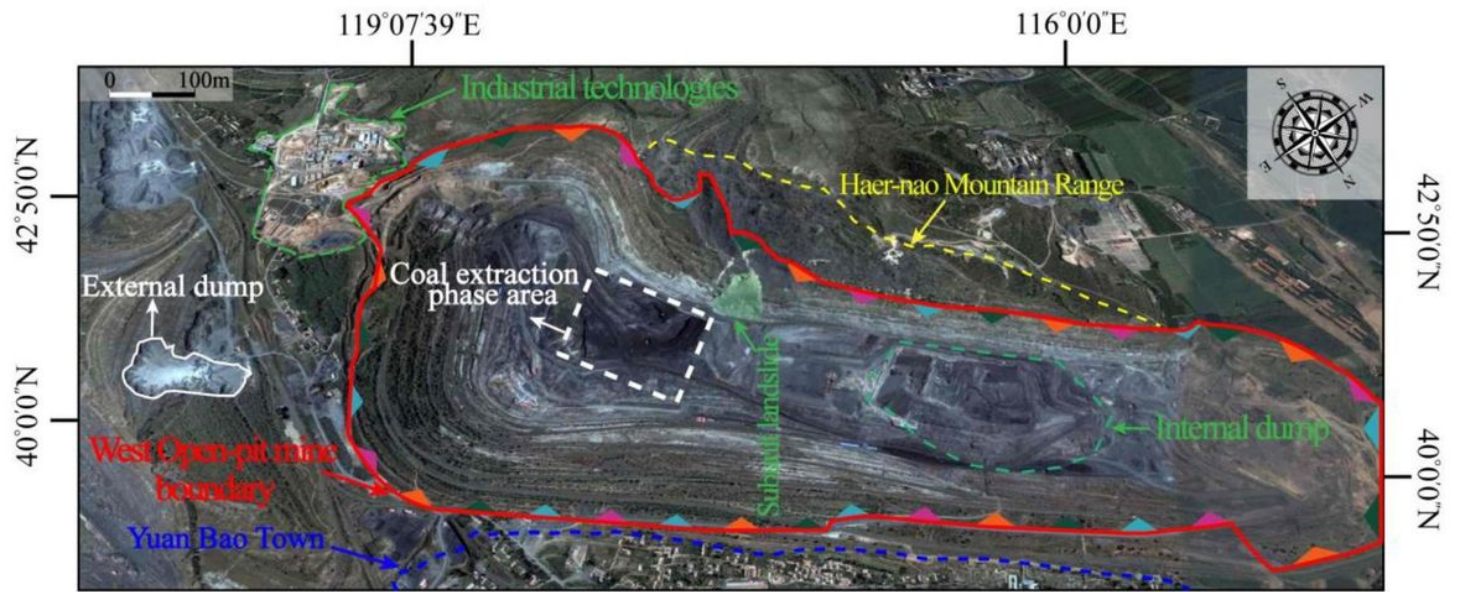


Figure 3

Orthoimage of Pingzhuang West Open-pit Mine

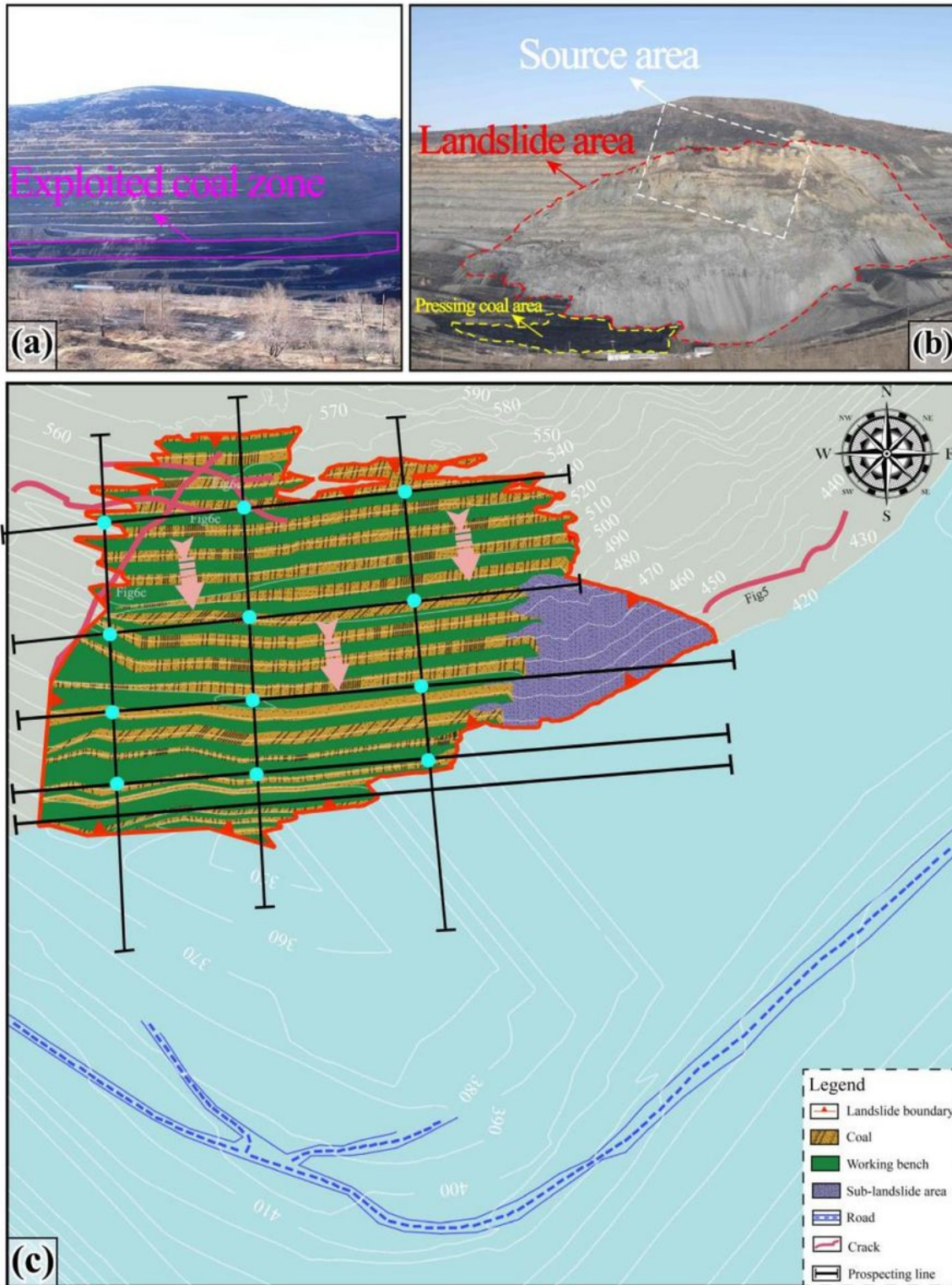


Figure 4

Landform and diagram of the open-pit mine landslide: (a) Front view of the slope pre sliding; (b) Front view of after landslide; (c) Planar map of the landslide.

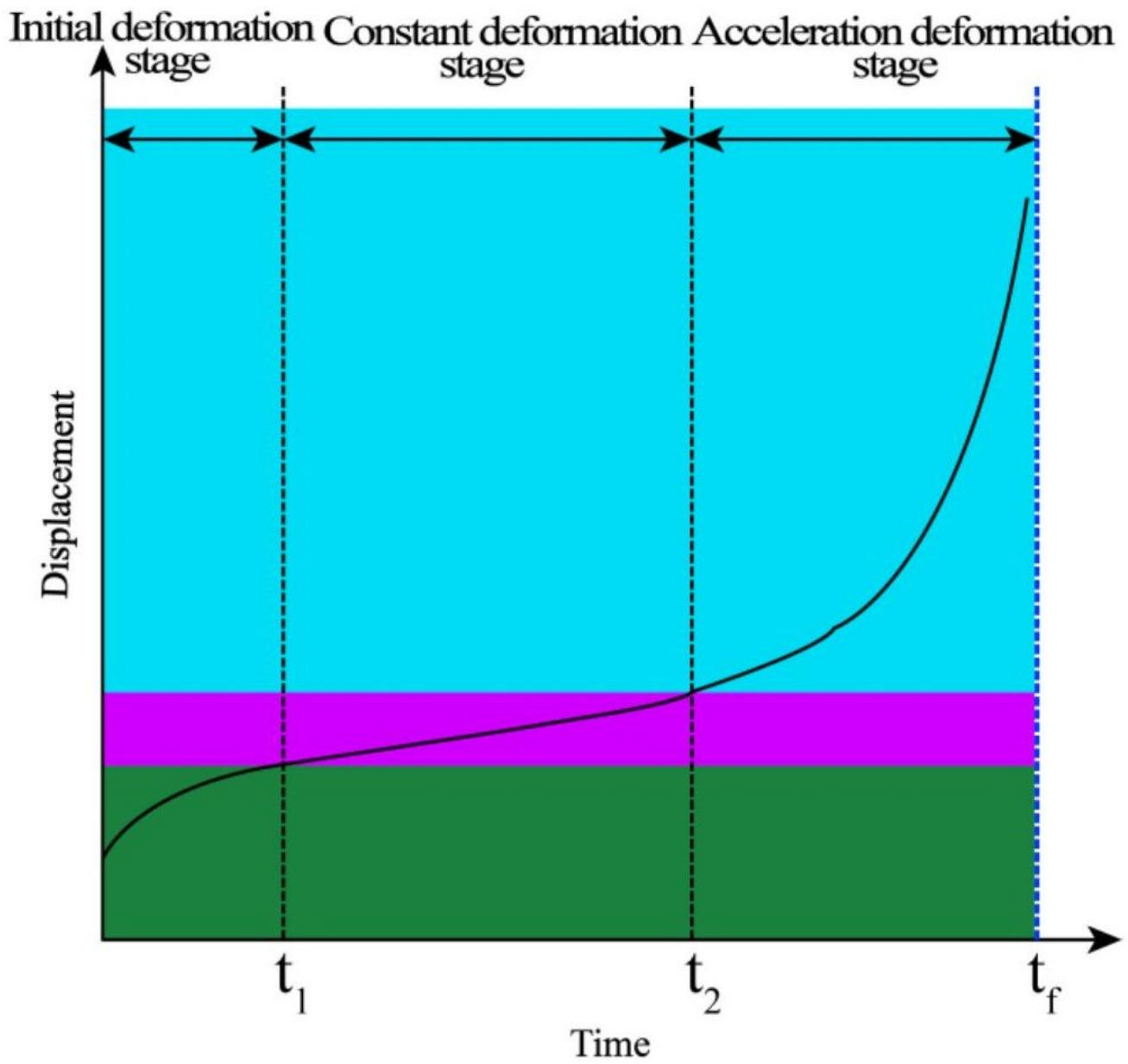


Figure 5

Diagram of three stages of landslide creep

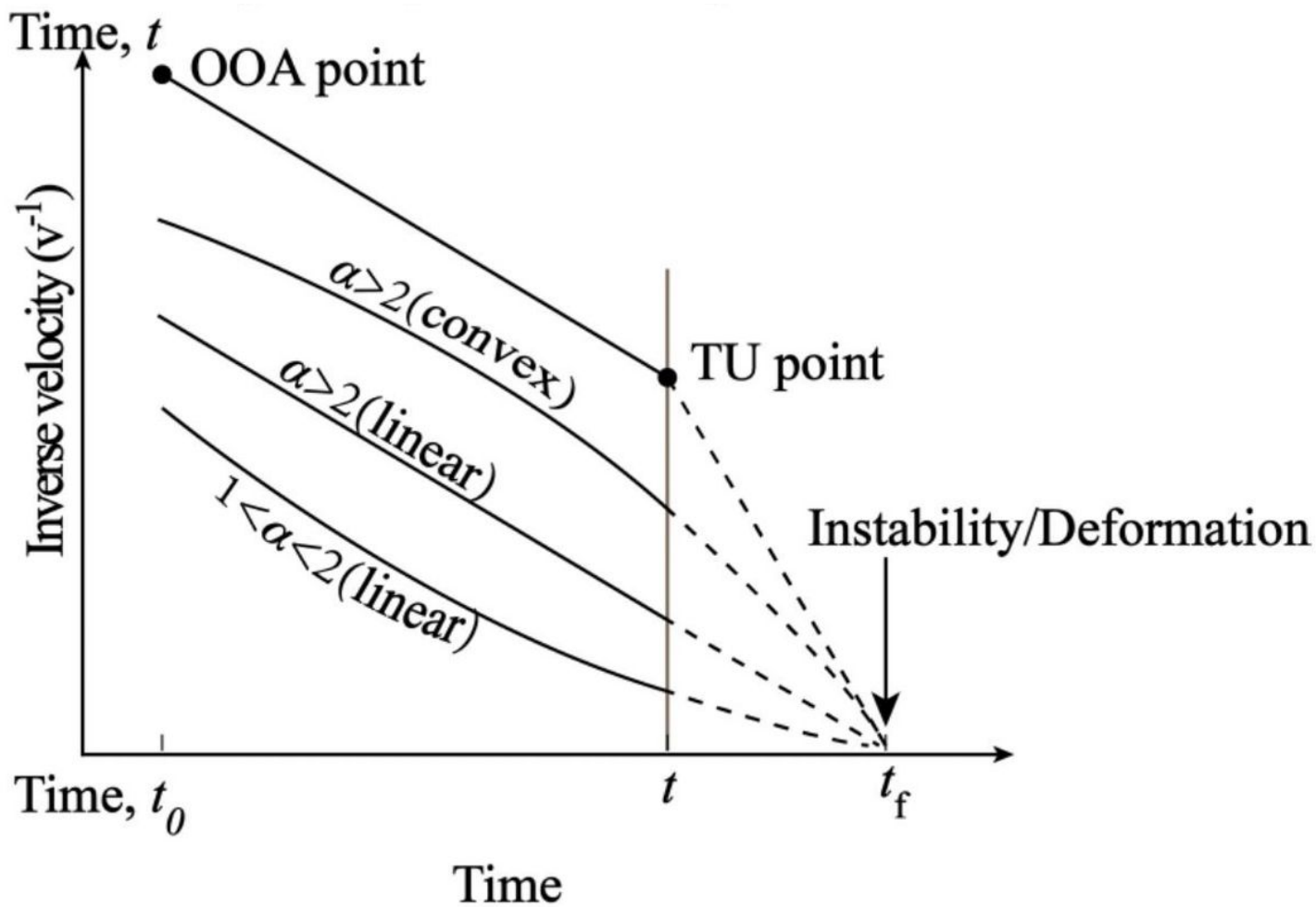


Figure 6

Schematic diagram of conventional inverse velocity method (modified after Chen and Jiang 2020). OOA is the onset of acceleration and TU is the trend update point.

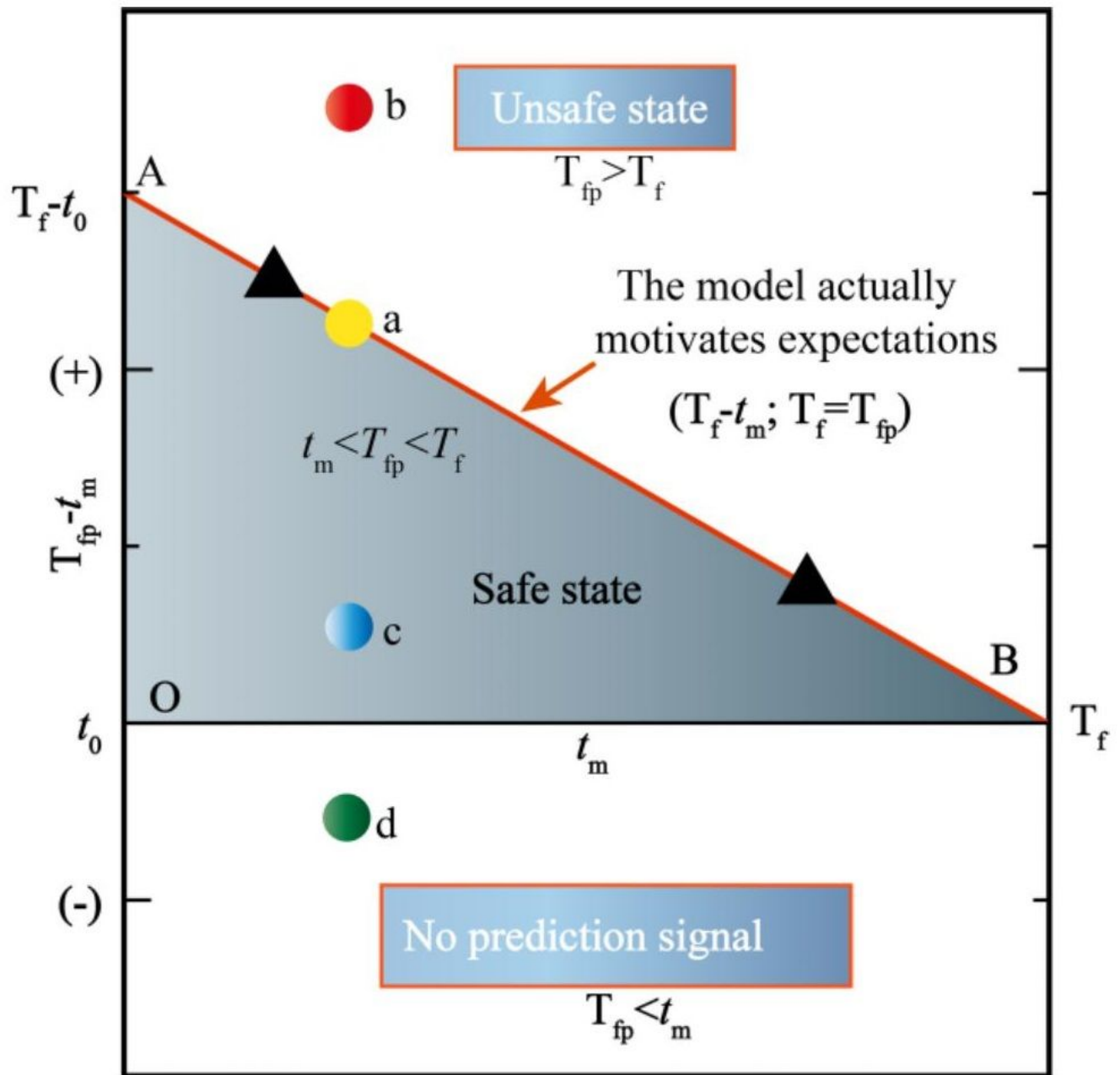


Figure 7

A basic theoretical model representing predicted life expectancy ($T_{fp} - t_m$) as a operation of t_m (time at instant of predicting) as failure-time T_f methods. Attention: t_0 is initial arbitrary time representing commencement of prediction and $T_f - t_0$ is initial actual life expectancy.

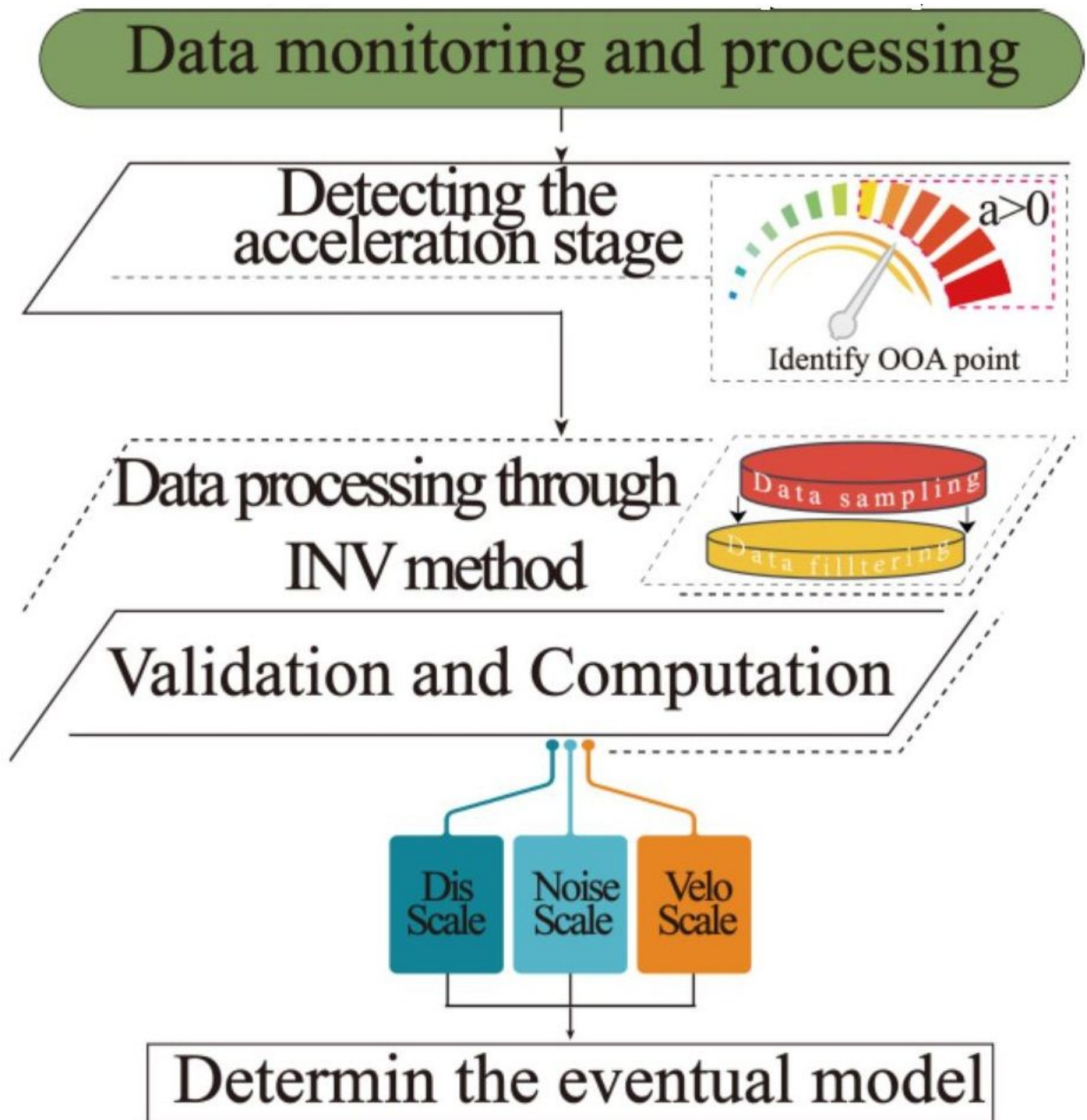


Figure 8

Flowchart for the real-time time-of-failure analysis methodology

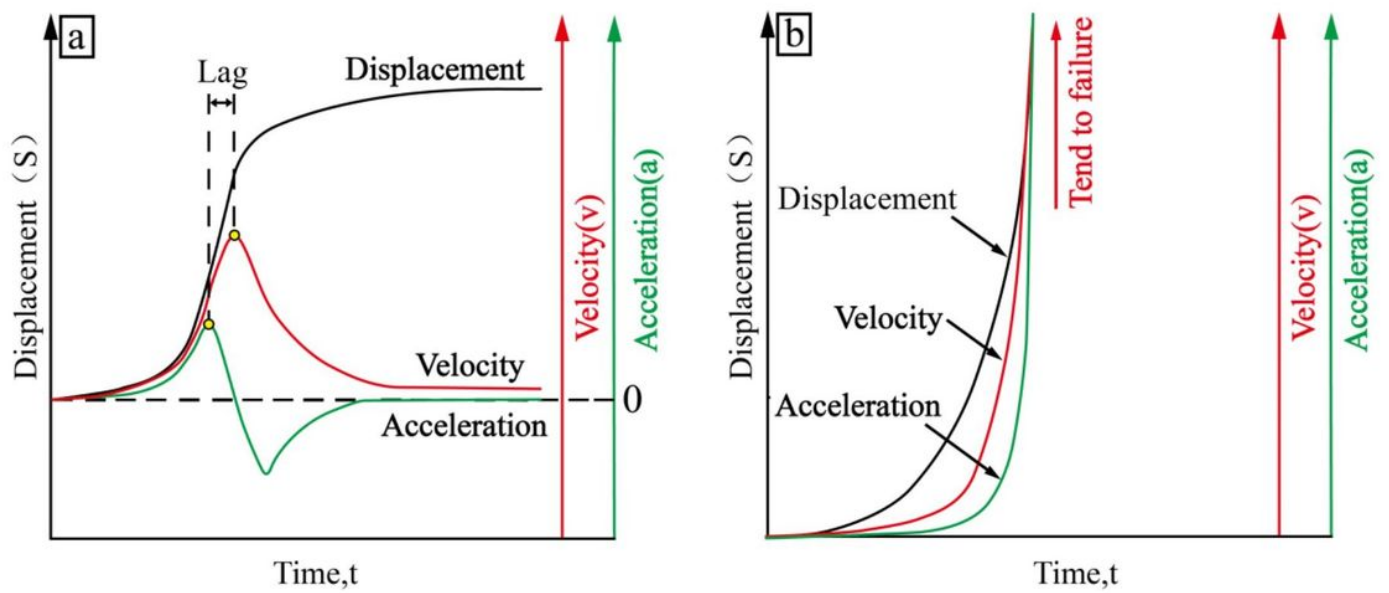


Figure 9

Schematic diagram of the relationship between displacement (S), velocity (v) and acceleration (a).

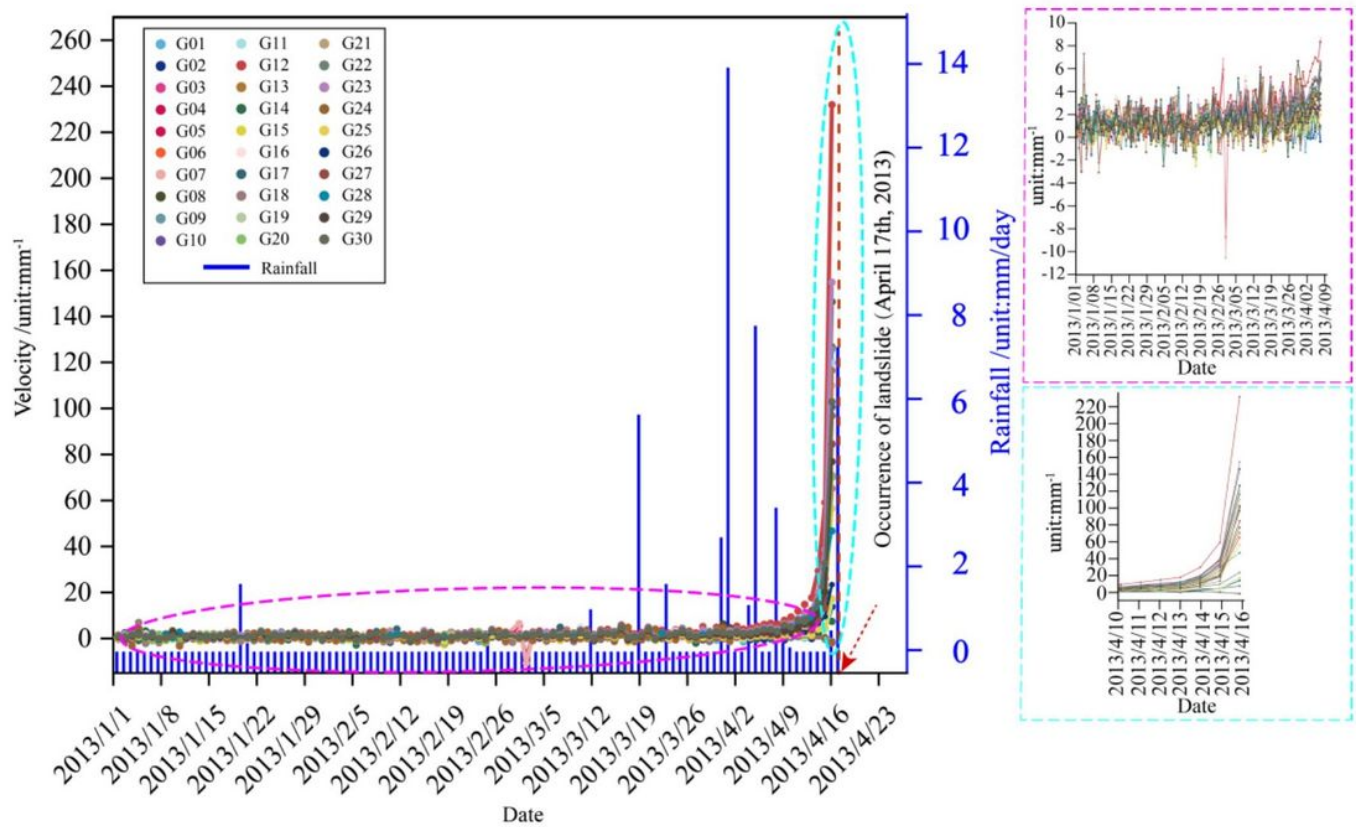


Figure 10

Velocity dataset and daily precipitation (grey) recorded at the Pingzhuang 4.17 landslide.

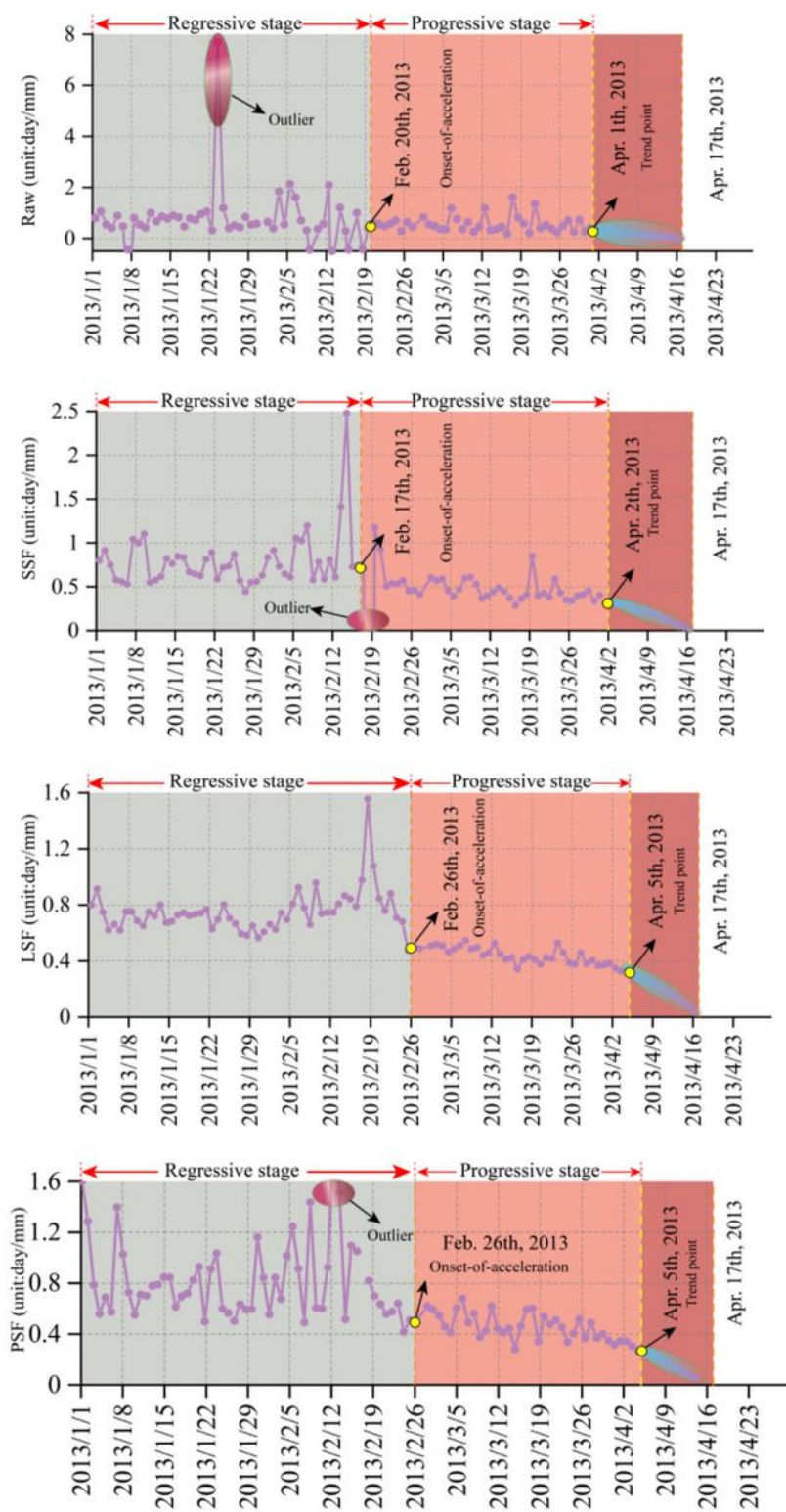
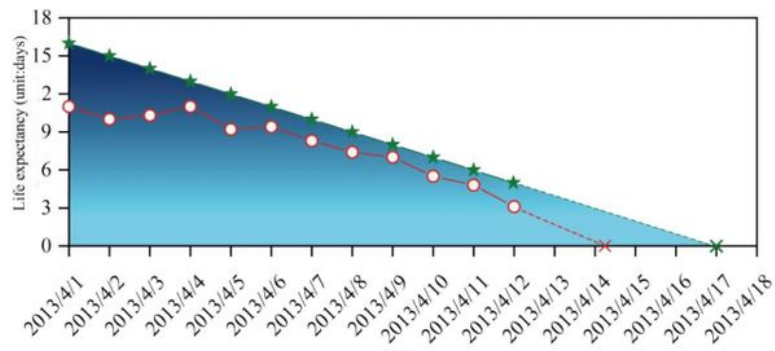
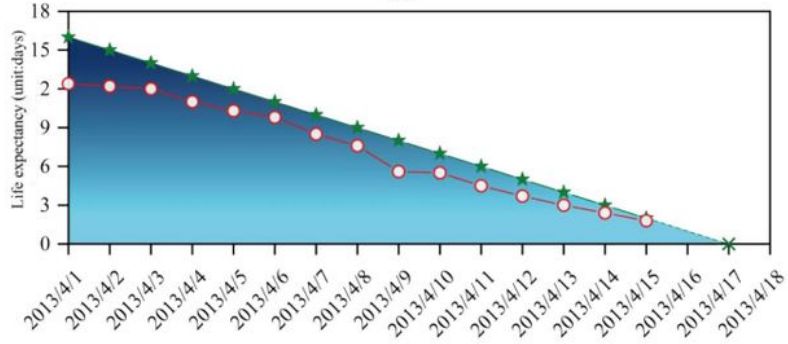


Figure 11

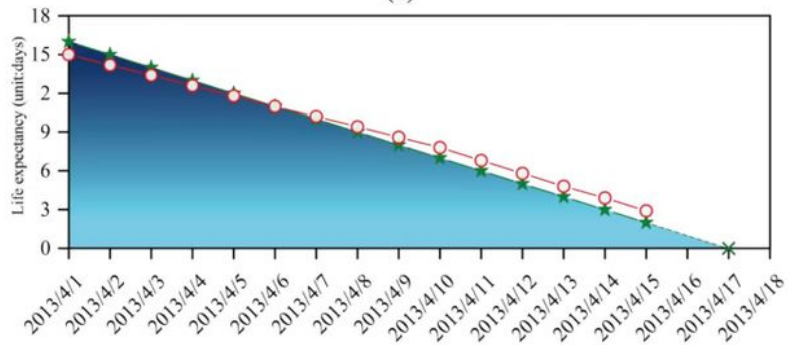
The representation method of landslide time prediction under inverse meta-model of velocity data multiplication



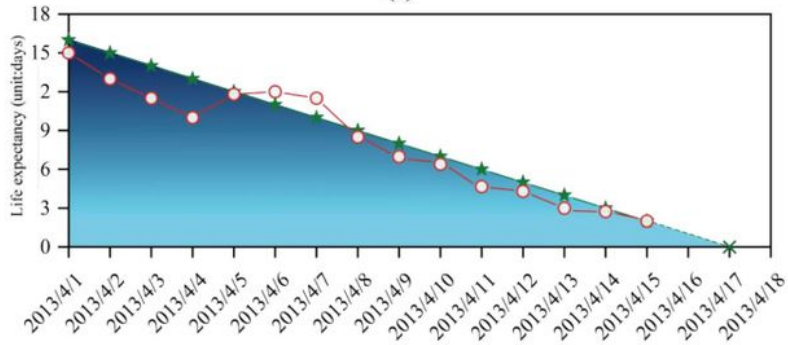
(a)



(b)



(c)



(d)

Figure 12

Life expectancy of Monitoring point 3300 in elevation 515

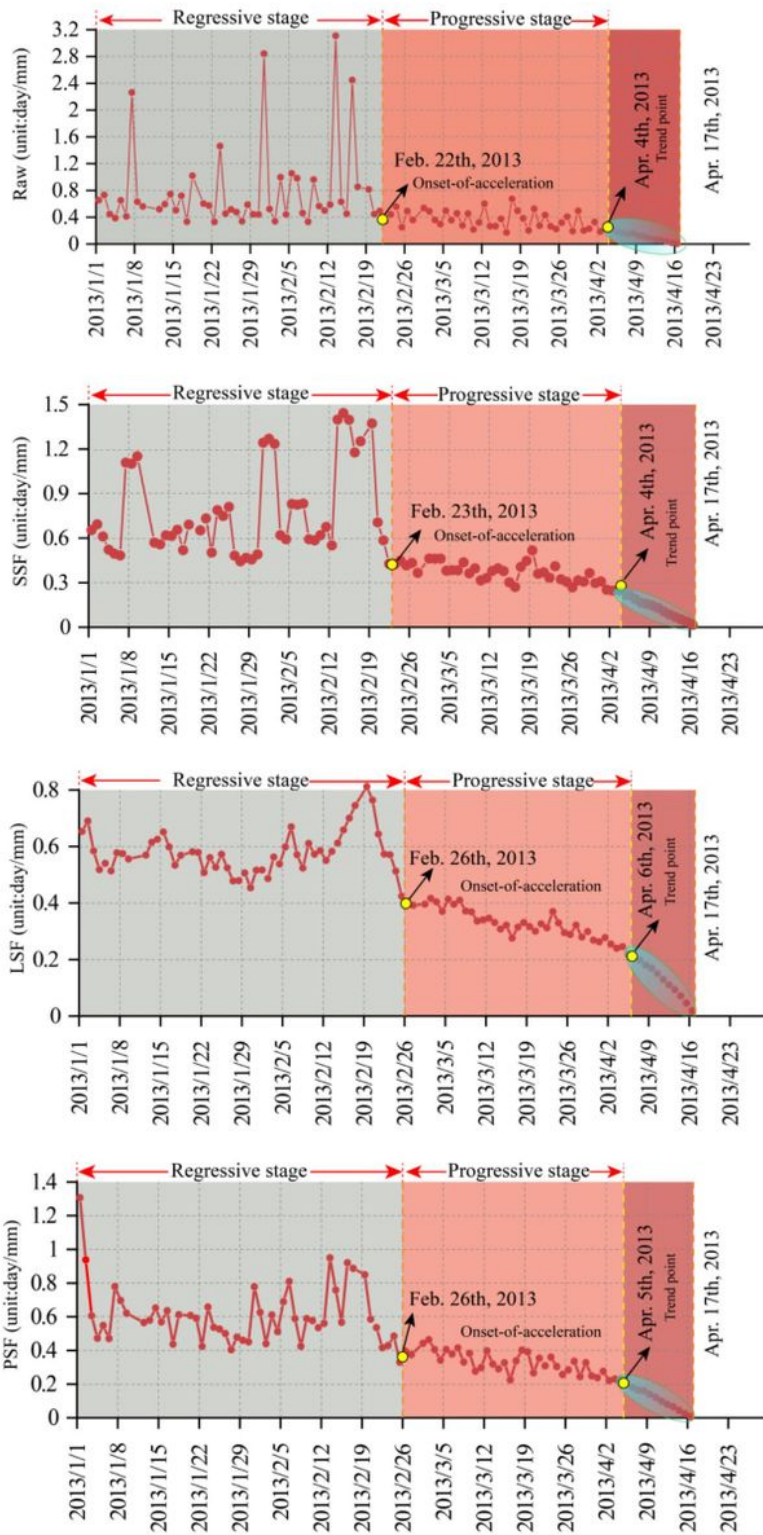
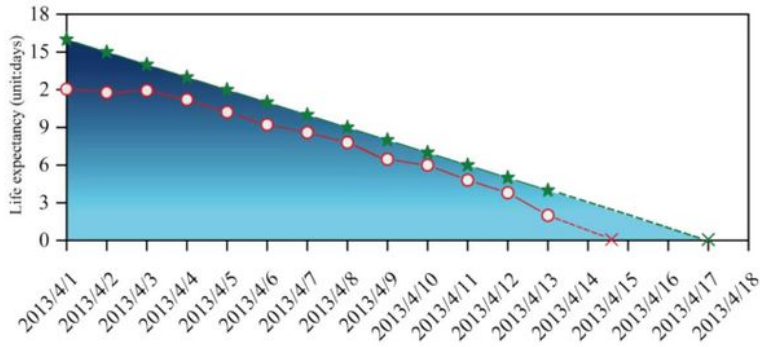
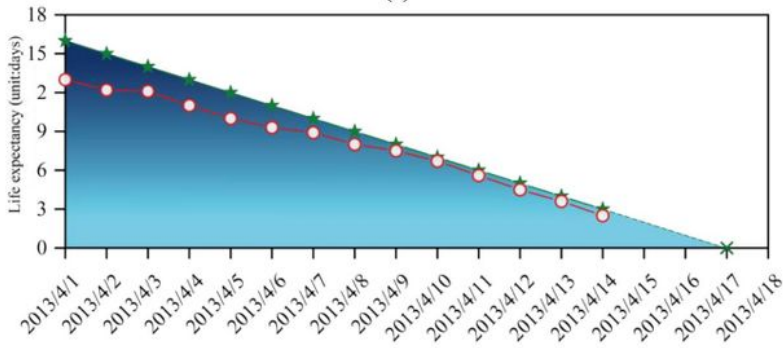


Figure 13

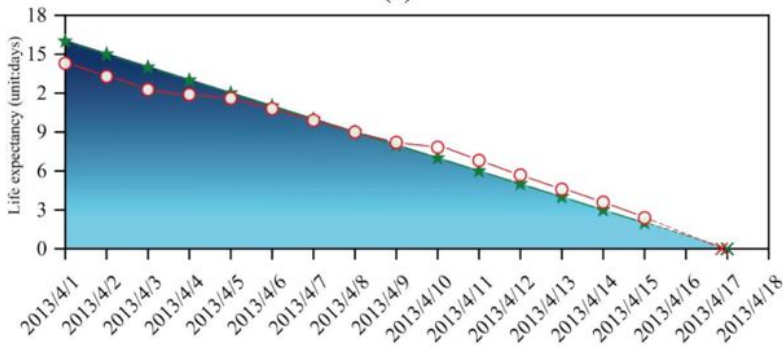
Schematic diagram of landslide time prediction based on reciprocal velocity data of 461-3250 time series model at monitoring points (a) Raw Data; (b) SSF; (c) LSF; (d) ESF.



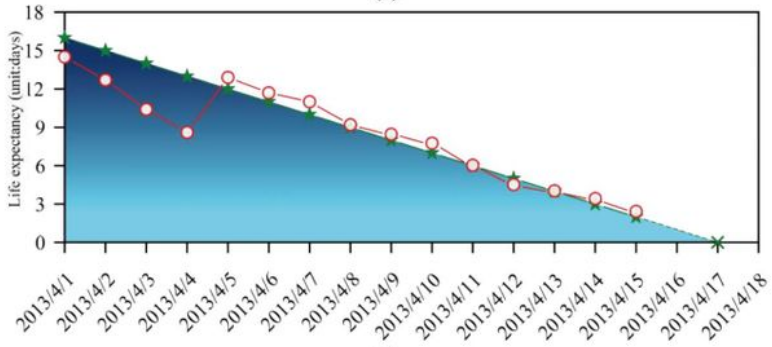
(a)



(b)



(c)



(d)

Figure 14

Life expectancy of Monitoring point 461 in elevation 3250

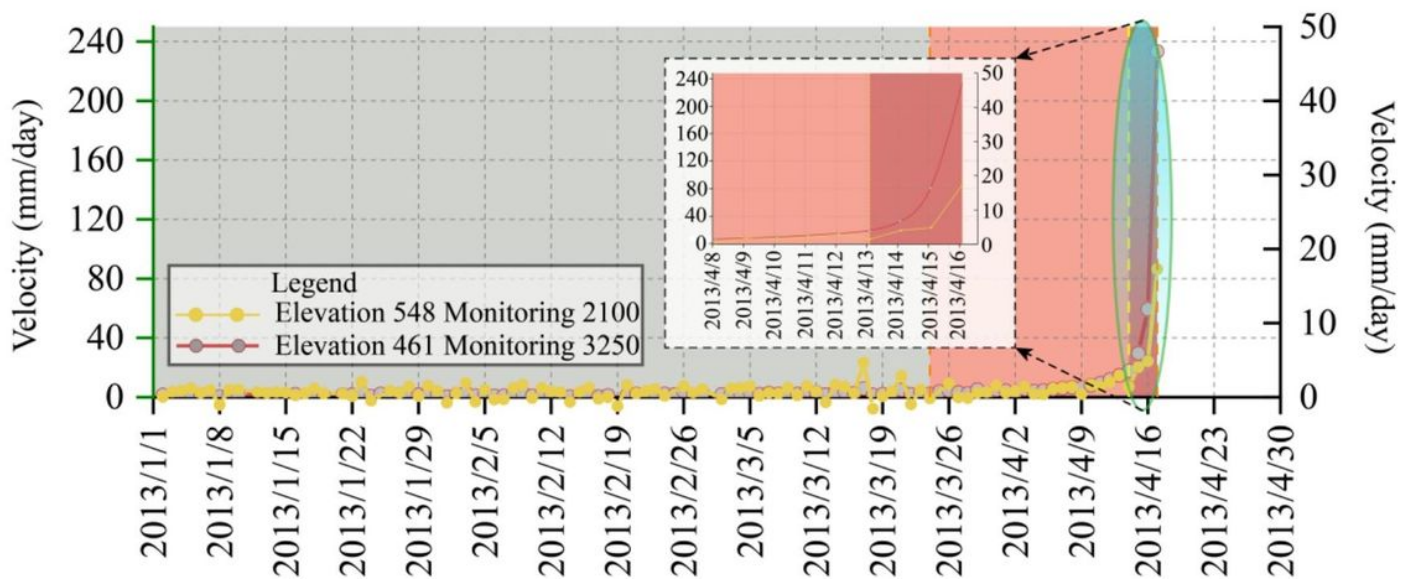


Figure 15

Diagram of displacement rate comparison of monitoring points 548-2100 and 461-3250

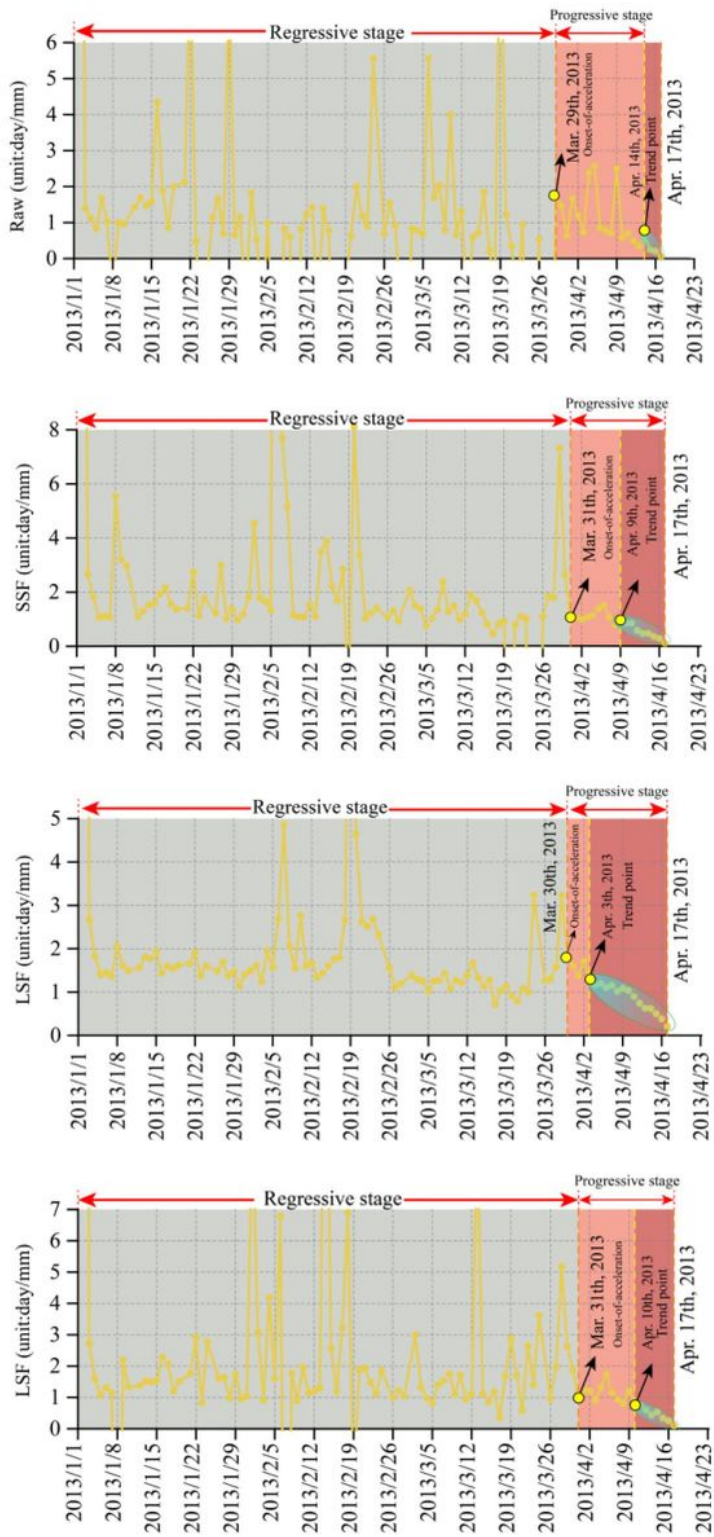
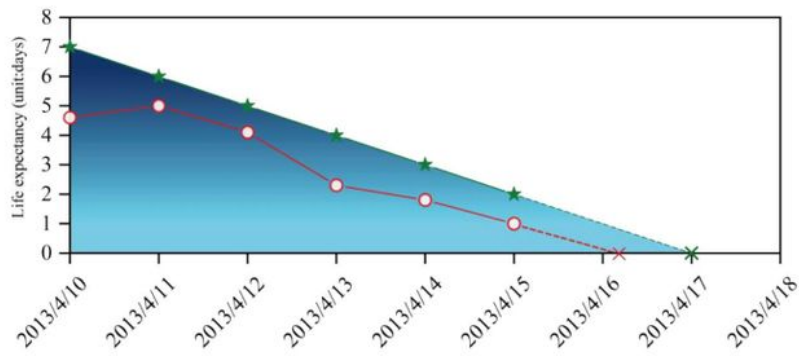
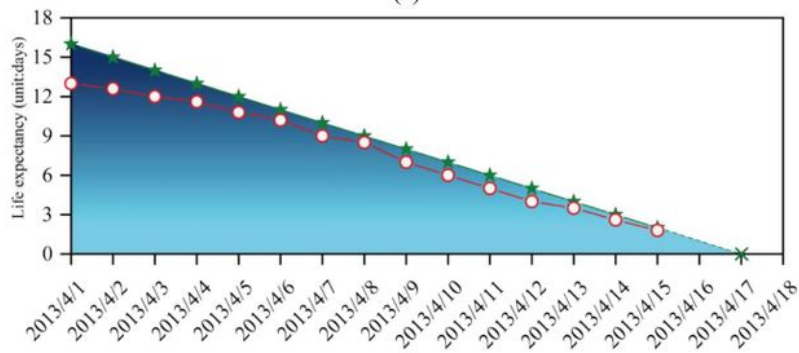


Figure 16

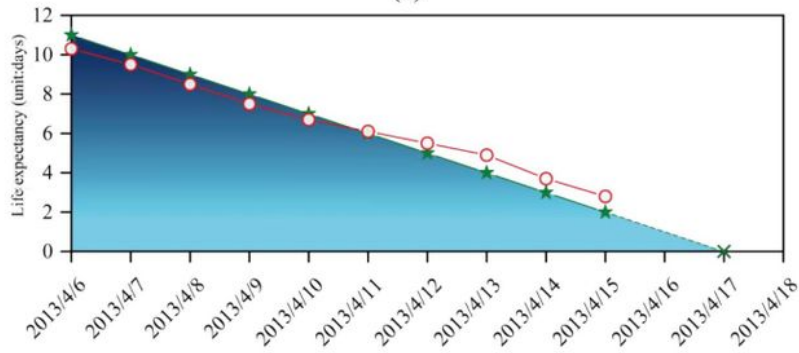
Schematic diagram of landslide time prediction based on reciprocal velocity data of 548-2100 time series model at monitoring points (a) Raw Data; (b) SSF; (c) LSF; (d) ESF.



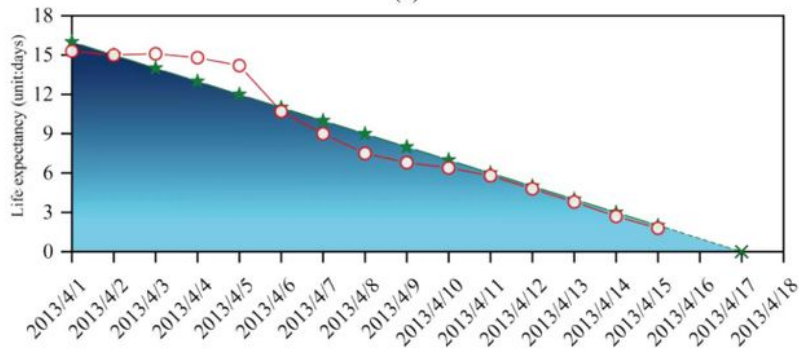
(a)



(b)



(c)



(d)

Figure 17

Life expectancy of Monitoring point 548 in elevation 2100

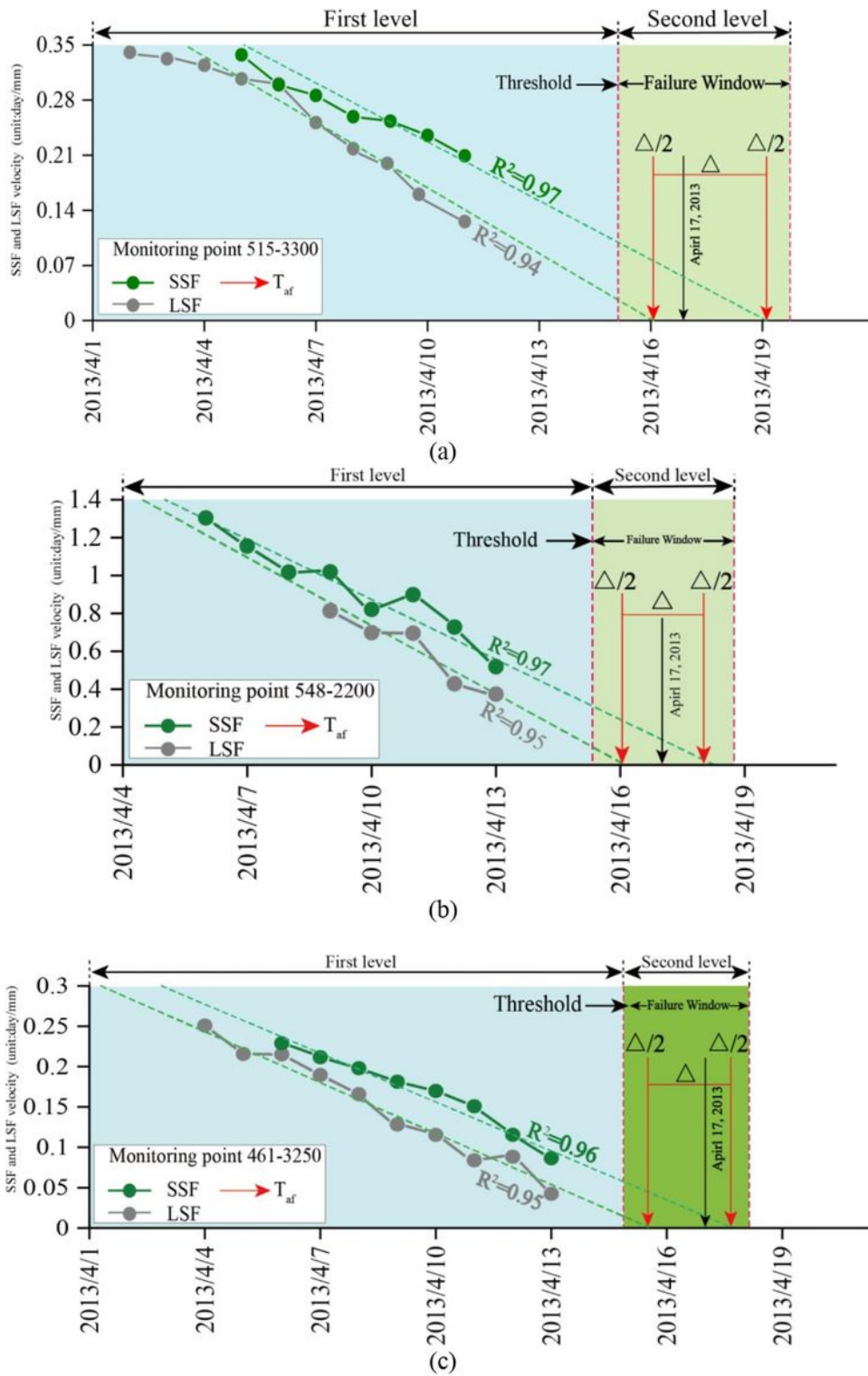


Figure 18

The time window expression of slope failure feedback from monitoring points 515-3300, 548-2200 and 461-3250